The Astrophysical Journal, 954:192 (15pp), 2023 September 10 https://doi.org/10.3847/1538-4357/acea83

Three-dimensional General-relativistic Simulations of Neutrino-driven Winds from Magnetized Proto–Neutron Stars

Dhruv K. Desai[1], Daniel M. Siegel[2,3,4], and Brian D. Metzger[1,5]
[1] Department of Physics and Columbia Astrophysics Laboratory, Columbia University, Pupin Hall, New York, NY 10027, USA
[2] Institute of Physics, University of Greifswald, D-17489 Greifswald, Germany
[3] Perimeter Institute for Theoretical Physics, Waterloo, Ontario N2L 2Y5, Canada
[4] Department of Physics, University of Guelph, Guelph, Ontario N1G 2W1, Canada
[5] Center for Computational Astrophysics, Flatiron Institute, 162 5th Ave., New York, NY 10010, USA
Received 2023 June 7; revised 2023 July 18; accepted 2023 July 24; published 2023 September 6

Abstract

Formed in the aftermath of a core-collapse supernova or neutron star merger, a hot proto–neutron star (PNS) launches an outflow driven by neutrino heating lasting for up to tens of seconds. Though such winds are considered potential sites for the nucleosynthesis of heavy elements via the rapid neutron capture process (*r*-process), previous work has shown that unmagnetized PNS winds fail to achieve the necessary combination of high entropy and/or short dynamical timescale in the seed nucleus formation region. We present three-dimensional general-relativistic magnetohydrodynamical simulations of PNS winds which include the effects of a dynamically strong ($B \gtrsim 10^{15}$ G) dipole magnetic field. After initializing the magnetic field, the wind quickly develops a helmet-streamer configuration, characterized by outflows along open polar magnetic field lines and a "closed" zone of trapped plasma at lower latitudes. Neutrino heating within the closed zone causes the thermal pressure of the trapped material to rise in time compared to the polar outflow regions, ultimately leading to the expulsion of this matter from the closed zone on a timescale of ∼60 ms, consistent with the predictions of Thompson. The high entropies of these transient ejecta are still growing at the end of our simulations and are sufficient to enable a successful second-peak *r*-process in at least a modest $\gtrsim$1% of the equatorial wind ejecta.

Unified Astronomy Thesaurus concepts: Magnetars (992); Neutron stars (1108); General relativity (641); Stellar winds (1636); R-process (1324); Supernova remnants (1667); High energy astrophysics (739)

1. Introduction

Magnetars are neutron stars with exceptionally high surface magnetic field strengths $\sim 10^{14}$–10^{15} G (e.g., Kouveliotou et al. 1998; Kaspi & Beloborodov 2017), which comprise $\gtrsim$30% of the young neutron star population (Woods & Thompson 2006; Beniamini et al. 2019). These strong magnetic fields affect the appearance of magnetars throughout their active lifetimes, for example by providing an additional source of heating due to magnetic dissipation and by powering transient outbursts and flares (e.g., Coti Zelati et al. 2018; Beniamini et al. 2019; CHIME/FRB Collaboration et al 2020). In this paper we shall explore one way in which such strong magnetic fields also affect the very first moments in a magnetar's life.

Whether formed from the core collapse of a massive star (e.g., Burrows et al. 1995; Janka et al. 2007), the accretion-induced collapse of a white dwarf (e.g., Dessart et al. 2006), or the merger of two neutron stars (e.g., Dessart et al. 2009; Giacomazzo & Perna 2013; Kaplan et al. 2014; Perego et al. 2014; Metzger et al. 2018), all neutron stars begin as hot "proto–neutron stars" (PNS; e.g., Burrows & Lattimer 1986; Pons et al. 1999), which cool and contract via optically thick neutrino emission for the first tens of seconds following their creation. As neutrinos stream outwards from the neutrinosphere through the atmosphere of the PNS, the heat they deposit in the surface layers drives a thermally driven outflow of baryons, known as a "neutrino-driven" wind (e.g., Duncan et al. 1986; Qian & Woosley 1996; Thompson et al. 2001). Neutrino-driven winds have received extensive interest as potential sites for the nucleosynthesis of rare heavy isotopes, particularly via the rapid neutron capture process (*r*-process; e.g., Meyer et al. 1992; Takahashi et al. 1994; Woosley et al. 1994). However, previous studies have shown that the roughly spherically symmetric winds from (slowly rotating, unmagnetized) PNSs fail to achieve the requisite combination of high entropy and short outflow expansion time through the seed nucleus formation region (Meyer et al. 1992; Hoffman et al. 1997; Meyer & Brown 1997) to enable the high ratio of neutrons to seeds necessary to achieve a successful second- or third-peak *r*-process (e.g., Kajino et al. 2000; Otsuki et al. 2000; Sumiyoshi et al. 2000; Thompson et al. 2001; Arcones et al. 2007; Fischer et al. 2010; Roberts et al. 2010; Arcones & Montes 2011; Fischer et al. 2012; Martínez-Pinedo et al. 2012; Roberts et al. 2012). Waves driven by convection, which steepen above the PNS surface and deposit additional entropy in the outflow, offer one possible mechanism to boost their *r*-process potential (e.g., Suzuki & Nagataki 2005; Metzger et al. 2007; Gossan et al. 2020; Nevins & Roberts 2023).

As prefaced above, most previous studies of PNS winds also neglect the impact of two other neutron star properties: rotation and magnetic fields. In recent work (Desai et al. 2022—hereafter Paper I) we explored the effects of rapid rotation on the wind properties by means of 3D general-relativistic (GR) hydrodynamic simulations. These simulations revealed that, while rapid rotation (spin periods $P \lesssim$ few milliseconds) acts to increase the mass-loss rate of the PNS near the rotational equator, the entropy and velocity of such outflows are suppressed compared to an otherwise equivalent nonrotating

star, precluding *r*-process production via an α-rich freeze-out. On the other hand, extremely rapid rotation approaching centrifugal breakout ($P \sim 1$ ms), was found to reduce the outflow electron fraction compared to the equivalent nonrotating wind model, thus potentially enabling the production of light *r*-process or light elementary primary process (LEPP) nuclei even absent an α-rich freeze-out.

The prevalence of such very rapidly spinning PNS in nature is not clear, however. Helioseismology observations and theoretical modeling suggest that angular momentum may be transferred out of the core of a massive star prior to core collapse with higher efficiency than had been previously assumed (e.g., Cantiello et al. 2016; Fuller et al. 2019). Another potential consequence of rapid birth rotation, which may limit its prevalence in nature, is to endow the PNS with a strong magnetic field $\gtrsim 10^{15}$ G via a dynamo process (e.g., Thompson & Duncan 1993; Price & Rosswog 2006; Siegel et al. 2013; Mösta et al. 2015; Raynaud et al. 2020; Reboul-Salze et al. 2022; White et al. 2022). While such "millisecond magnetars" formed in magnetorotational core-collapse supernovae (e.g., Bugli et al. 2021; Obergaulinger & Aloy 2021; Bugli et al. 2023 for recent works) or neutron star mergers (e.g., Kiuchi et al. 2018; Mösta et al. 2020; Combi & Siegel 2023b) are contenders for the central engines behind energetic transients such as engine-powered supernovae and gamma-ray bursts (e.g., Usov 1992; Wang et al. 2001; Thompson et al. 2004; Bucciantini et al. 2007; Metzger et al. 2007; Bucciantini et al. 2009; Metzger et al. 2011; Prasanna et al. 2023), these explosions are so rare as to represent at most only a tiny fraction of all magnetar births (e.g., Vink & Kuiper 2006; Fuller & Lu 2022). Nevertheless, if such objects exist, recent works studying the dynamics and nucleosynthesis of magnetorotational supernovae find that the combination of rapid rotation and magnetic fields can indeed give rise to conditions that would allow for second- and potentially third-peak *r*-process element production (e.g., Winteler et al. 2012; Kuroda et al. 2020; Reichert et al. 2023).

On the other hand, rapid rotation may not be the only mechanism to generate magnetar-strength fields, which in principle could originate from flux freezing from the precollapse stellar core (Woltjer 1964; Ruderman 1972; Ferrario & Wickramasinghe 2006; Cantiello et al. 2016) or dynamos during the PNS phase which require less extreme core angular momentum (Barrère et al. 2022; White et al. 2022). This motivates considering the effects of a strong magnetic field on PNS birth even in the absence of rapid rotation.

In this work (Paper II) we perform general-relativistic magnetohydrodynamical (GRMHD) simulations which explore the impact of strong ($B \gtrsim 10^{14}$–10^{15} G) dipole magnetic fields on the properties of neutrino-heated outflows from nonrotating PNS winds. We are motivated by the work of Thompson (2003), who showed that a magnetar-strength field can initially trap plasma close to the PNS surface, where it can be heated by neutrinos to a higher entropy than achieved in an otherwise equivalent freely outflowing wind. Thompson & ud-Doula (2018) studied this problem numerically by means of 2D axisymmetric MHD simulations with Newtonian gravity, using an approximate inner boundary condition near the PNS neutrinosphere and a prescribed free-streaming neutrino radiation field above. They found that a moderate fraction $\sim$1%–10% of the wind material may be ejected in high-entropy outflows capable of *r*-process via an α-rich freeze-out. Likewise, Prasanna et al. (2022) performed similar simulations but covering a wider parameter space of the neutrino-driven winds from slowly rotating magnetars, focusing on the effects that neutrino-driven mass loss has in opening magnetic field lines and enhancing the star's spin-down rate relative to the magnetic dipole rate. Our goal here is to explore a similar setup using 3D GRMHD simulations including neutrino transport via an M0 scheme, thus paving the way for future simulations within this numerical setup that include both magnetic fields and rapid rotation together.

This paper is organized as follows. In Section 2 we introduce the numerical code and model runs. In Section 3, we compare outflows from magnetars of various magnetic field strengths. In Section 4 we summarize and compare our results to outflows from unmagnetized winds, and further discuss the viability of *r*-process nucleosynthesis in magnetar winds.

2. Methodology

2.1. Numerical Evolution Code, PNS Initial Data, and Grid Setup

We perform GRMHD simulations of magnetized PNS winds using a modified version of `GRHydro` (Mösta et al. 2014) as described in Siegel & Metzger (2018), built on the open-source `Einstein Toolkit`[6] (Goodale et al. 2003; Schnetter et al. 2004; Thornburg 2004; Löffler et al. 2012; Babiuc-Hamilton et al. 2019). The initial conditions reflect the state of a PNS in its cooling phase ($\sim$1 s postbounce, e.g., Figure 3 of Roberts & Reddy 2017), following the end of the dynamical accretion phase responsible for forming the PNS. As in Paper I, we do not evolve spacetime for the current models. Instead, we evolve the GRMHD equations on a fixed background metric, determined at the start of the simulation by our initial data solver, for computational efficiency. This assumption is justified by the fact that only a tiny fraction $\sim 10^{-5}$ of the star's mass is removed over the course of the simulation and the total energy in the magnetic field is $\lesssim 10^{-7}$ of the star's gravitational energy.

We include weak interactions via a leakage scheme based on the formalism of Bruenn (1985) and Ruffert et al. (1996), following the implementation in Galeazzi et al. (2013) and Radice et al. (2016; see also Siegel & Metzger 2018). In the presence of strong magnetic fields, the neutrino heating and cooling rates will be altered with respect to an unmagnetized setup, due to the impact of Landau quantization on the available electron/positron states (e.g., Lai & Qian 1998; Duan & Qian 2004). However, as we show in Appendix A.4, these effects are small, even for the strongest magnetic field strength cases explored in this work. We are thus justified in neglecting these corrections.

As in Paper I, we employ a one-moment approximation to the GR Boltzmann equation ("M0") to describe neutrino transport. It is implemented as a ray-by-ray scheme (Radice et al. 2016) in our enhanced version of `GRHydro`, in which the neutrino mean energies and number densities are evolved along null radial coordinate rays (see also Combi & Siegel 2023a). The M0 radiation transport grid is separate from that of the GRMHD variables. It uses spherical coordinates centered on the PNS, uniformly spaced in $\{r, \theta, \phi\}$ extending out to radii of 200 km, with the number of grid points $(n_r, n_\theta, n_\phi) = (600, 20,$

[6] http://einsteintoolkit.org

40). It thus covers the density range $\rho \gtrsim 10^4$ g cm^{-3}, for which weak interactions are relevant, to ensure accuracy of the model (see Paper I for more details).

Our magnetized PNS models use as initial conditions unmagnetized PNS wind solutions similar to those presented in Paper I, run sufficiently long for the wind to achieve a quasi steady state, but short compared to the Kelvin–Helmholtz cooling timescale of the PNS. These unmagnetized wind solutions are then endowed with a large-scale dipolar magnetic field (see Section 2.2 for more details). Here, we briefly review the setup of the unmagnetized models.

The initial conditions for the PNS structure are determined by the Tolman–Oppenheimer–Volkoff equations, employing a density-dependent initial temperature and Y_e profile (computed by imposing β equilibrium), following the approach by Kaplan et al. (2014). We use the SFHo equation of state (Steiner et al. 2013) in tabular form as provided by O'Connor & Ott (2010).[7] We do not self-consistently follow the PNS cooling evolution to arrive at the initial conditions for our models; thus the final electron fraction Y_e in the outflows, which depends sensitively on the neutrinosphere properties, will not be physically accurate. Nevertheless, we can draw conclusions regarding the effects (if any) of strong magnetic fields on the wind composition by comparing Y_e from our magnetized models to those obtained from otherwise equivalent unmagnetized models.

Our fiducial model employs a grid hierarchy consisting of a base Cartesian grid and six fixed nested refinement levels. We improve upon the resolution used in the models from Paper I. The smallest and finest grid is a $15 \times 15 \times 15$ km box centered at the origin now with a resolution of 150 m, while the size of the base grid is $960 \times 960 \times 960$ km. As discussed in Paper I, this grid setup allows us to capture the wind zone simultaneously on scales of ∼100–1000 km, while providing enough resolution from the finest grid to capture the details of the outflows from the PNS surface. For this resolution, the magnetic pressure scale height $H_{p_B} = |d \ln p_B/dr|^{-1}$ is resolved by at least 10 grid points throughout the entire domain of the simulation (see Appendix A.1, Figure 15). As in Paper I, the neutrinosphere is only marginally resolved, with the grid resolution approximately equal to the optical depth scale height (see Appendix A.1, Figure 15). This issue is not critical for the purposes of this study, as the neutrino energies and luminosities determined at the neutrinosphere serve as a boundary condition for the heating that occurs at larger radii, a region that by comparison is well resolved. Most of our calculations employ reflection symmetry across the equatorial ($z = 0$) plane for computational efficiency. We have checked that our results for the time-averaged wind properties are not appreciably affected by this assumption, by performing a full-domain simulation and a side-by-side comparison to the half-domain case (see Appendix A.2).

2.2. Addition of a Dipole Magnetic Field

We evolve the unmagnetized PNS and its wind for ∼150 ms, the last ∼50 ms over which the wind has achieved a quasi steady state. At this point, we superimpose a large-scale magnetic field onto the stationary wind solution. As in Siegel et al. (2014) and similar to the configurations in Shibata et al. (2011) and Kiuchi et al. (2012), we define this large-scale,

[7] https://stellarcollapse.org/equationofstate.html

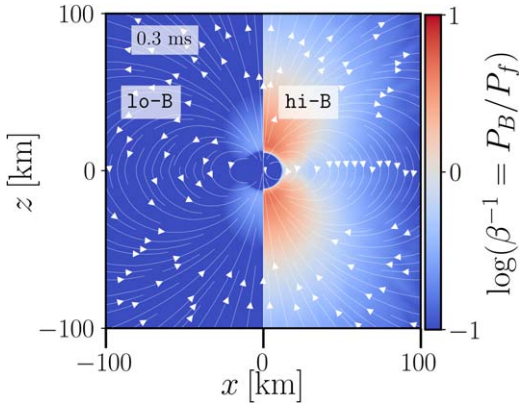

Figure 1. Initial magnetic-to-fluid pressure ratio β^{-1} with magnetic field line geometry overlaid. We show models `lo-B` (left) and `hi-B` (right) in a slice through the magnetic dipole axis ($y = 0$ plane), soon after the magnetic field is turned on at $t = 0$ ms. This magnetic field configuration was added onto an unmagnetized PNS wind solution previously evolved for about 176 ms to steady state. For model `hi-B`, magnetic pressure dominates over fluid pressure in the polar regions above the PNS surface out to ≈60 km.

dipole-like magnetic field by initializing the components of the vector potential as $A_r = A_\theta = 0$, and

$$A^\phi = A_{0,d} \frac{\varpi_{0,d}/\sqrt{2}}{(r^2 + \varpi_{0,d}^2/2)^{3/2}}, \quad (1)$$

where $A_{0,d}$ tunes the overall field strength, ϖ is the cylindrical radius, $r^2 = \varpi^2 + z^2$, and $\varpi_{0,d} \simeq 8$ km is the "neutral point." The neutral point corresponds to a ring-like current in the equatorial ($z = 0$) plane centered at the origin. We require this neutral point to lie within the star (of radius $R_{\rm PNS} \simeq 12$ km) so as to yield a plausible, nearly point-like dipole field that is nonsingular everywhere. The magnetic field is then obtained via $B = \nabla \times A$, yielding the initial configuration shown in Figure 1. The dipole geometry is symmetric across the $z = 0$ plane at initialization. Although the current sheet that forms in this plane can "wobble," we find that when averaged over time, these wobbles smooth out (Figure 16 of Appendix A.2). Hence, the time-averaged wind outflow properties should also be roughly symmetric across the $z = 0$ plane, justifying our use of equatorial symmetry for computational efficiency.

We activate the magnetic field after running the unmagnetized PNS wind evolution for roughly ≈176 ms, at which point we "reset" the clock and hereafter refer to this time as $t = 0$. In order to explore different physical regimes of the magnetized winds, we consider models which span two different initial surface magnetic field strengths but are otherwise identical. We distinguish these models by their polar magnetic field strength $B_{\rm S}$ at the neutrinosphere, with $B_{\rm S} \simeq [6.1 \times 10^{14}$ G, 2.5×10^{15} G], referred to as `lo-B` and `hi-B`, respectively (see Table 1 and Figure 1 for further details). In addition to the magnetized models, we run in parallel an unmagnetized model ($B_{\rm S} = 0$, referred to as `no-B`), which provides a set of comparison wind properties over the same time interval (i.e., for the same PNS neutrino cooling evolution).

The magnetic field does not significantly impact the hydrostatic structure of the PNS. At the time the field is initialized, the magnetic-to-fluid pressure ratio $\beta^{-1} \equiv P_B/P_f$ obeys $<10^{-2}$ for all the models we consider (see Figure 1). This ratio similarly shows that the gradient of the magnetic

Table 1
Suite of PNS Wind Simulations: Magnetic Field and Neutrino Properties

Model	B_S[a] (10^{15} G)	R_e[b] (km)	$R_{\bar{\nu}_e}$[c] (km)	$\langle L_{\nu_e}\rangle$[d] (erg s^{-1})	$\langle L_{\bar{\nu}_e}\rangle$[e] (erg s^{-1})	$\langle E_{\nu_e}\rangle$[f] (MeV)	$\langle E_{\bar{\nu}_e}\rangle(g)$ (MeV)
no-B[h]	0.0	13	10	2.2e51	3.9e51	13	18
lo-B	0.61	13	10	2.2e51	3.9e51	13	18
hi-B	2.5	13	10	2.3e51	3.8e51	13	18
sym-B[i]	2.1	13	11	4.3e51	6.0e51	13	17
no-sym-B[i]	2.2	13	11	4.1e51	6.8e51	13	18

Notes.
[a] Magnetic field strength as measured along the polar axis at the radius of the $\bar{\nu}_e$ neutrinosphere.
[b] Initial equatorial radius of the star.
[c] Steady-state $\bar{\nu}_e$ neutrinosphere radius.
[d] Luminosities and mean energies of electron neutrinos and antineutrinos, averaged over the final factor of three in simulation time.
[h] Fiducial unmagnetized wind model (Figure 2, left panels).
[i] All simulations employ the same grid geometry, but these models are run with three times poorer resolution compared to the models in the first three rows (i.e., $\Delta x = 450$ m for the finest grid).

field is negligible with respect to the fluid pressure gradient. The magnetic field is not dynamically relevant; only the wind region is potentially impacted by its presence.

The toroidal component of the magnetic field remains subdominant compared to the poloidal component at all epochs and for all models (see Appendix A.3). This is expected because the initial magnetic field configuration is purely poloidal and there is no significant active mechanism, such as rotation, winding up magnetic fields on large scales.

3. Results

The presence of a magnetic field can significantly impact the dynamics of the PNS wind in regions where the magnetic pressure $P_B = B^2/8\pi$ greatly exceeds the fluid pressure P_f (Thompson 2003; Thompson & ud-Doula 2018; Prasanna et al. 2022). In the gain region just above the PNS surface, where neutrino heating begins to exceed neutrino cooling, the radiation pressure of photons and electron/positrons dominates over the gas pressure and hence $P_f \simeq P_{\rm rad} = (11/12)aT^4$, where a is the radiation constant. Just below this point closer to the star, the specific neutrino-heating rate $\propto L_\nu \epsilon_\nu^2/r^2$ and neutrino cooling rate $\propto T^6$ (due to pair-capture reactions on free nucleons) balance, resulting in a roughly isothermal atmosphere of temperature (e.g., Qian & Woosley 1996)

$$T_{\rm eq} \approx 1\ L_{\bar{\nu}_e,51}^{1/6} \langle E_{\bar{\nu}_e,\rm MeV}\rangle^{1/3} R_{\bar{\nu}_e,6}^{-1/3}\ \rm MeV, \quad (2)$$

where $R_{\bar{\nu}_e} = R_{\bar{\nu}_e,6} \times 10^6$ cm , $L_{\bar{\nu}_e} = L_{\bar{\nu}_e,51} \times 10^{51}$ erg s^{-1}, and $\langle E_{\bar{\nu}_e}\rangle = \langle E_{\bar{\nu}_e,\rm MeV}\rangle \times$ MeV are the PNS radius, electron antineutrino luminosity, and mean electron antineutrino energy, respectively.

Equation (2) reveals that $P_B > P_{\rm rad}$ for magnetic field strengths above the critical value

$$B_{\rm crit} \approx 7 \times 10^{14}\ \rm G \left(\frac{L_{\bar{\nu}_e,51}}{4}\right)^{\frac{1}{3}} \left(\frac{E_{\bar{\nu}_e}}{18\ \rm MeV}\right)^{\frac{2}{3}} \left(\frac{R_{\bar{\nu}_e}}{10\ \rm km}\right)^{-\frac{2}{3}}. \quad (3)$$

Thus, for surface dipole fields $B_S \gg B_{\rm crit}$ we expect the wind dynamics to be significantly altered by the presence of the magnetic field.

We begin in Section 3.1 by presenting results for a relatively weakly magnetized model (lo-B), for which $B_S < B_{\rm crit}$ and hence the wind dynamics are expected to be similar to the unmagnetized wind. In Section 3.2, we move on to describing a strongly magnetized model (hi-B) for which $B_S > B_{\rm crit}$ and discuss the prospects for r-process nucleosynthesis in Section 3.3.

3.1. Weakly Magnetized Model

The left panel of Figure 1 shows the magnetic-to-fluid pressure ratio $\beta^{-1} = P_B/P_f$ and magnetic field line geometry for the weakly magnetized model lo-B at the moment of magnetic field initialization. Figure 2 shows a comparison of the key quantities from the magnetized and unmagnetized models (lo-B and no-B, respectively) 55 ms after a weak magnetic field is turned on.

Before the magnetic field is activated, the PNS wind has achieved an approximately steady state, as detailed in Paper I. At the moment the magnetic field is initialized, the magnetic field lines reflect a dipole geometry and the $\beta^{-1} = P_B/P_f$ of the wind is $\lesssim 1$, indicating that fluid pressure dominates over magnetic pressure from the start (Figure 1). As the wind subsequently evolves, the dipole magnetic field structure is disrupted, as evidenced by the field line geometry at late times (Figure 3, left panel). The magnetic field is "frozen in" within the radial fluid flow (see the velocity field in Figure 2, bottom panel). By $\sim$55 ms after magnetic field initialization, the outflows in models lo-B ($B_S = 6.1 \times 10^{14}$ G) and no-B ($B_S = 0$) are nearly indistinguishable (Figure 2).

Because the fluid pressure exceeds the magnetic pressure upon magnetic field initialization nearly everywhere ($\beta^{-1} < 1$ in Figure 1, left), and since the magnetic field lines are frozen into the fluid flow, the magnetic field lines follow the mostly radial outflow of the neutrino-driven wind. The magnetic field thus tears open from its initial dipole configuration within milliseconds, approaching a split-monopole configuration (see the left panel of Figure 3). For such a split-monopole solution, $B(r) \propto r^{-2}$, rather than $B(r) \propto r^{-3}$, as for dipole geometry (e.g., Weber & Davis 1967). This is illustrated in Figure 4, which shows angle-averaged radial profiles of the poloidal magnetic field strength in the polar region for models lo-B and hi-B at the time the magnetic field is initialized (solid lines, for which $B(r) \propto r^{-3}$) as well as $\sim$30 ms later (dashed lines, for which $B(r) \propto r^{-2}$). A thin "current sheet" region forms in the equatorial plane with a low magnetic-to-fluid pressure ratio β^{-1} as the wind evolves to $t \approx 55$ ms (Figure 3, left panel). Here, the magnetic field lines of opposite polarities from the

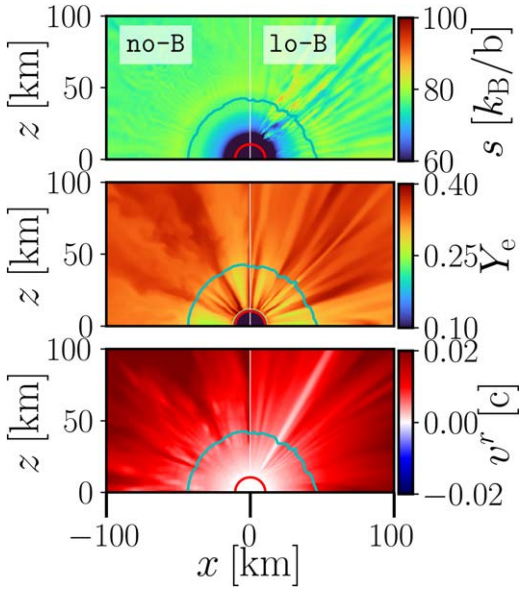

Figure 2. Snapshots showing the outflow properties as a cross section through the magnetic dipole axis ($y = 0$ plane) at $t \approx 55$ ms after B-field initialization for models `no-B` (unmagnetized, left) and `lo-B` (weakly magnetized, right). From top to bottom: specific entropy s, electron fraction Y_e, and radial velocity v^r. The green contour represents the α-particle formation surface ($X_\alpha = 0.5$), around which r-process seed nuclei begin to form, while the red contour represents the location of the neutrinosphere ($\tau_{\bar{\nu}_e} = 1$ surface).

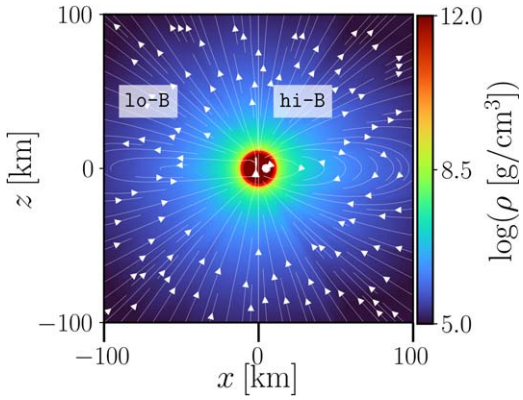

Figure 3. Snapshots of the outflow properties as a cross section through the magnetic dipole axis ($y = 0$ plane) at $t \approx 55$ ms after B-field initialization for models `lo-B` (left) and `hi-B` (right). Colors show the rest-mass density ρ, with the magnetic field line geometry overlaid in white. The neutrinosphere ($\tau_{\bar{\nu}_e} = 1$ surface) is shown with a red contour. The field lines have been nearly completely torn open radially in the weakly magnetized model, while an equatorial belt of closed field lines persists in the strongly magnetized case.

northern and southern hemispheres reconnect and heat the fluid (however, note that the physical thickness of the current sheet is not resolved by the simulation because the resistivity is numerical in this ideal MHD setup).

Aside from the magnetic field properties, all of the asymptotic wind properties remain largely unaffected compared to the prior unmagnetized state. The PNS hydrostatic structure and neutrino energies as well as luminosities are essentially unchanged with respect to the unmagnetized model (see Table 1). Consequently, the net specific heating rate $\dot{q}_{\rm net}$, which depends on the neutrino properties and temperature, retains a similar radial profile. After an initial transient phase, the outflow properties of model `lo-B`, such as the specific entropy s, electron fraction Y_e, and radial velocity v^r, and the

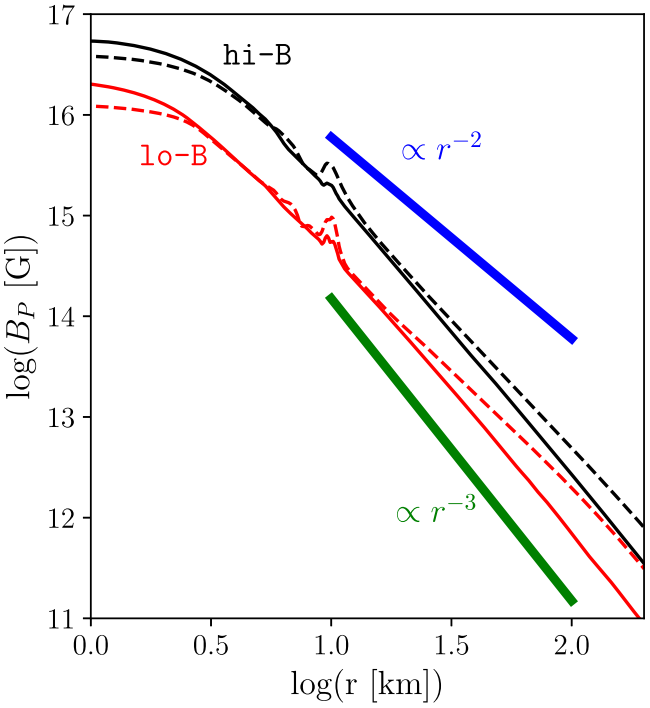

Figure 4. Radial profiles of the poloidal magnetic field strength $B_{\rm P}$ for models `lo-B` and `hi-B`, taken from a slice through the magnetic dipole axis ($y = 0$), angle averaged in the polar region from $\theta = 0°$ to $\theta = 45°$. Solid lines show $B_{\rm P}$ time averaged from $t \approx 0$–5 ms after the magnetic field is activated, while dashed lines represent $B_{\rm P}$ time averaged from $t \approx 25$–35 ms. To guide the eye, thick solid lines show power laws of r^{-2} (blue) and r^{-3} (green). Both models approach the split-monopole solution ($\propto r^{-2}$) in the polar region.

asymptotic wind properties are also very similar to the `no-B` model (Figure 2, Table 2).

Because the temperature and density profiles change little after the magnetic field is activated, the surface at which α-particles form (roughly where $T \lesssim 5 \times 10^9$ K) remains at $r \approx 45$ km, close to the outer edge of the gain region (Figure 2). As outlined by Qian & Woosley (1996) and reviewed in Paper I, the ability of the PNS wind to generate r-process nuclei yields depends on s, Y_e, and the expansion timescale $t_{\rm exp}$, which we define as

$$t_{\rm exp} = \left(v^r \frac{\ln dT}{dr} \right)^{-1} \Bigg|_{X_{\rm nuc}=0.5}, \quad (4)$$

where we have defined $X_{\rm nuc} = 0.5$ as the α-particle surface ($X_{\rm nuc}$ is the mass fraction of all nuclei excluding protons and neutrons), as typically located 50–100 km above the PNS surface. In particular, the r-process figure of merit defined by Hoffman et al. (1997)

$$\eta \equiv \frac{s^3}{Y_e^3 t_{\rm exp}}, \quad (5)$$

is a rough measure of success for heavy element nucleosynthesis due to α-rich freeze-out, where here and hereafter $t_{\rm exp}$ is measured in seconds and s is measured in $k_{\rm B}$ per baryon. Threshold values of $\eta \gtrsim 4 \times 10^9$ and $\eta \gtrsim 9 \times 10^9$ are required for neutron capture to proceed to the second and third r-process peaks, respectively. As found in Paper I, and consistent with past findings (e.g., Qian & Woosley 1996; Hoffman et al. 1997; Thompson et al. 2001), unmagnetized PNS winds (model

Table 2
Time-averaged Outflow Properties

Model	Sector[i]	$\langle \dot{M} \rangle_{60\ \mathrm{km}}$[a] ($M_\odot\ \mathrm{s}^{-1}$)	$\langle \dot{E}_K \rangle_{60\ \mathrm{km}}$[b] (erg s^{-1})	$\langle s \rangle_{60\mathrm{km}} \pm \sigma_s$[c] k_B baryon^{-1}	$\langle t_{\mathrm{exp}} \rangle_{60\ \mathrm{km}} \pm \sigma_{t_{\mathrm{exp}}}$[d] (ms)	$\langle Y_e \rangle_{60\ \mathrm{km}} \pm \sigma_{Y_e}$[e]	$\langle \eta \rangle_{60\mathrm{km}} \pm \sigma_\eta$[f] ($10^8$)
no-B[g]	tot.	5.5e-5	5.4e45	78 ± 0.9	20 ± 9	0.40 ± 0.003	5.6 ± 2
lo-B	tot.	5.6e-5	5.1e45	78 ± 1.9 (78→78)	21 ± 6	0.36 ± 0.003	5.3 ± 2 (5.2→5.3)
hi-B	tot.	3.8e-5	3.1e45	82 ± 5	29 ± 20	0.37 ± 0.002	5.1 ± 4
hi-B	pol.	2.9e-5	2.3e45	80 ± 4 (80→80)	32 ± 10	0.37 ± 0.002	3.8 ± 2 (3.5→3.9)
hi-B	equat.	4.3e-5	3.6e45	84 ± 6 (83→85)	25 ± 20	0.37 ± 0.02	6.5 ± 4 (5.7→7.8)
sym-B[h]	tot.	1.6e-4	3.6e46	67 ± 3	16 ± 10	0.38 ± 0.02	4.6 ± 2
no-sym-B[h]	tot.	1.8e-4	5.4e46	68 ± 3	21 ± 40	0.38 ± 0.03	4.6 ± 3

Notes. We report wind properties time averaged from $t \approx 25$–55 ms for models no-B, lo-B, and hi-B, and from $t \approx 0$–20 ms for models sym-B and no-sym-B. Entries of the format ($q \rightarrow q'$) refer to the same quantity time averaged from $t \approx 25$–35 ms (q) and from $t \approx 45$–55 ms (q').

[a] Isotropic mass-loss rate.

[b] Kinetic energy.

[c] Specific entropy with standard deviation.

[d] Expansion timescale with standard deviation.

[e] Electron fraction with standard deviation.

[f] r-process figure of merit $\eta \equiv s^3/(Y_e^3 t_{\mathrm{exp}})$ with standard deviation.

[g] Fiducial unmagnetized wind model shown in Figure 2 (left-hand panels).

[h] All simulations in the table use the same grid geometry, but these models are run with a third of the resolution compared to the models in the first three rows (i.e., $\Delta x = 450$ m for the finest grid).

[i] Quantities are averaged over different angular sectors in polar angle θ: "equat." ($45° \leqslant \theta \leqslant 135°$), "pol." ($0° \leqslant \theta \leqslant 45°$ and $135° \leqslant \theta \leqslant 180°$), and "tot." ($0° \leqslant \theta \leqslant 180°$). Isotropic-equivalent quantities are reported for $\langle \dot{M} \rangle$ and $\langle \dot{E}_K \rangle$ at a radius $r = 60$ km.

no-B) generally have $\eta \ll 1 \times 10^9$, insufficient for an r-process. Not surprisingly then, our weakly magnetized model lo-B is also not capable of an r-process (Table 2).

3.2. Strongly Magnetized Model

We now consider the results for the strongly magnetized model (hi-B) with $B_{\mathrm{S}} = 2.5 \times 10^{15}\ \mathrm{G} > B_{\mathrm{crit}}$. Immediately after the magnetic field is activated, its dipole geometry is identical to that of model lo-B, with the poloidal field strength following the expected r^{-3} radial profile (Figure 4). The magnetic-to-fluid pressure ratio, however, is much larger compared to the weakly magnetized model, reaching $\beta^{-1} \sim 10$ near the polar regions for model hi-B (Figure 1). Right after the magnetic field is initialized, the radial velocity v^r is negative in a region extending from slightly above the neutrinosphere at $r \approx 15$ km to $r \approx 50$ km, as a result of the previously outflowing wind plasma being trapped by the strong magnetic field.

The mass-loss rate $\dot{M}$ through a fixed surface of radius ≈60 km is also suppressed after the magnetic field is initialized ($t \approx 0$) by almost a factor of 2 from its original value, from $\dot{M} \approx 5.6 \times 10^{-5}\ M_\odot\ \mathrm{s}^{-1}$ to $\dot{M} \approx 3.2 \times 10^{-5}\ M_\odot\ \mathrm{s}^{-1}$ (top panel of Figure 5). Dividing the outflow into separate polar ($\theta = 0°$–$45°$ and $135°$–$180°$) and equatorial ($\theta = 45°$–$135°$) angular sectors, we see that the isotropic-equivalent mass-loss rate $\dot{M}_{\mathrm{iso}}$ along the equatorial direction has returned to its original value by $t \approx 35$ ms and continues to increase, approaching $\dot{M}_{\mathrm{iso}} \approx 10^{-4} M_\odot\ \mathrm{s}^{-1}$ by $t \approx 55$ ms. By contrast, $\dot{M}_{\mathrm{iso}}$ in the polar region remains significantly suppressed for the entirety of the simulation. As we describe below, this suppression is the result of the extra work the polar outflows must perform to open the field lines in this region and escape to infinity.

As shown in Figure 6, the radial velocity remains small or negative $|v^r| \ll 0.01c$ in the equatorial region between $r \approx 15$ km and $r \approx 100$ km, indicating the presence of a sustained "trapped zone" at low latitudes. The magnetic-to-fluid pressure ratio β^{-1} begins to rise in the polar region and to drop in the equatorial region (Figure 7). At the same time, the specific entropy in the $\theta = 60°$–$120°$ equatorial trapped belt between $r = 15$ km and $r = 100$ km rises from $s \approx 75$ to $s \approx 100$ by $t \approx 55$ ms (Figure 8).

Since magnetic fields do not strongly impact the hydrostatic structure of the PNS atmosphere near the neutrinosphere, neither the neutrino luminosities/energies nor the neutrinosphere radii are altered significantly by the magnetic field (Table 1). Insofar as the neutrino fluxes and energies determine the relative rate of ν_e and $\bar{\nu}_e$ absorption by the wind material, the wind's electron fraction is not altered considerably compared to the unmagnetized model (Figure 9). The density and temperature profiles, particularly of the inner hydrostatic atmosphere, also remain only mildly affected by the presence of the magnetic field (Figure 10).

As discussed at the beginning of Section 3, the impact of the magnetic field on the wind dynamics can be understood in terms of the high magnetic-to-fluid pressure ratio in model hi-B (Figure 1, right panel). Outflowing matter in the polar regions tear open originally closed magnetic field lines, resulting in a split-monopole geometry at high latitudes (similar to that achieved across all outflow directions in model lo-B). Given that the surface magnetic field strength is fixed, the transformation from $B \propto r^{-3}$ to $\propto r^{-2}$ by ≈30 ms (Figure 4) causes the magnetic-to-fluid pressure ratio above the surface at high latitudes to increase with time.

In addition, matter that would otherwise have traveled radially in the polar region is partially redirected along magnetic field lines, which bend toward lower latitudes. This suppresses $\dot{M}_{\mathrm{iso}}$ in the polar region (Figure 5, top panel, dashed line). Field lines at midlatitudes ($\theta \approx 30°$–$60°$ and $120°$–$150°$) are gradually opened ("peeled off" from originally closed field lines at low latitudes) and the pressure ratio there similarly increases (Figure 7). In the equatorial region ($\theta \approx 60°$–$120°$), however, magnetic tension remains high enough to oppose

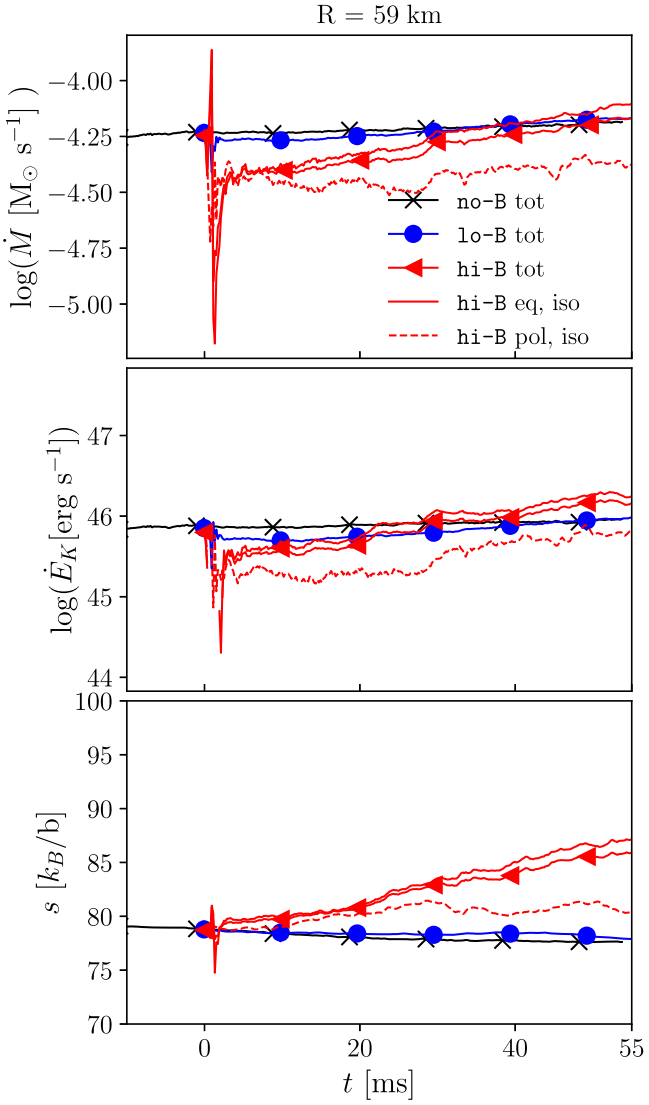

Figure 5. Mass-loss rate $\dot{M}$ (top), kinetic power $E_K = (W-1)\dot{M}$ (center), where W is the Lorentz factor, and $\dot{M}$-weighted average specific entropy s (bottom) of the outflows through a spherical surface of radius $r = 60$ km, as a function of time since magnetic field initialization. For all models, `no-B` (black, ×), `lo-B` (blue circles), and `hi-B` (red triangles), these quantities are shown across the full 4π solid angle. For model `hi-B` (red), we show separately the isotropic-equivalent mass-loss rate as well as the kinetic power, and the average entropy across a solid angle at high latitudes close to the poles ($\theta = 0°$–$45°$ and $\theta = 135°$–$180°$; dotted line) and near the equatorial plane ($\theta = 45°$–$135°$; solid line).

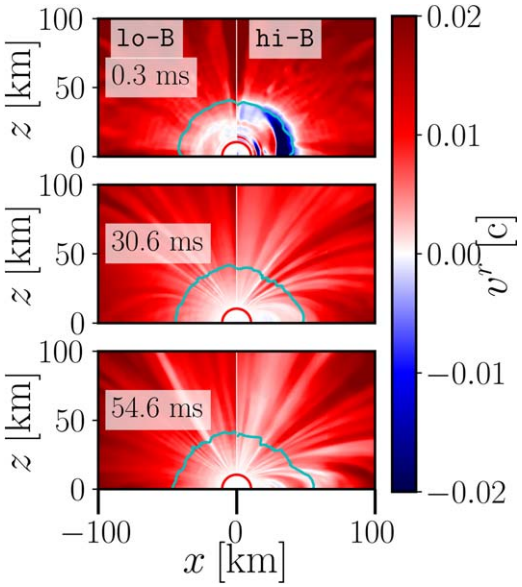

Figure 6. Snapshots of the radial velocity v^r in the $y = 0$ magnetic dipole axis plane for models `lo-B` and `hi-B`. The top panel shows the moment the magnetic field is initialized ($t \approx 0$ ms), while the middle and bottom panels are at $t \approx 31$ ms and $t \approx 55$ ms, respectively. A cyan contour represents the α-particle formation surface ($X\alpha = 0.5$) around which r-process seed nuclei begin to form, while the red contour represents the neutrinosphere surface ($\tau_{\bar{\nu}_e} = 1$). The lower velocities of matter in the equatorial closed zone region, particularly in the first two snapshots, are apparent.

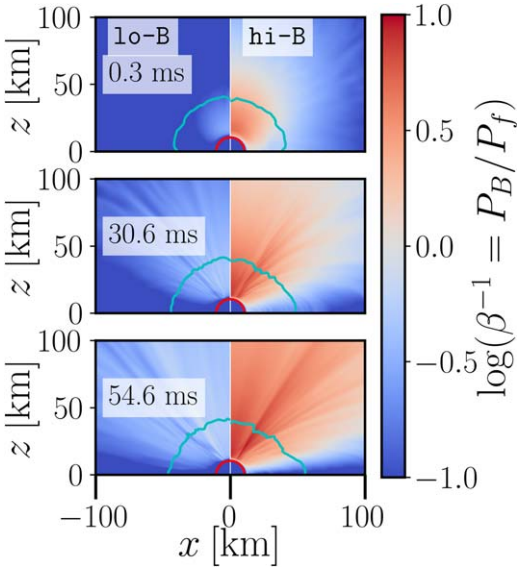

Figure 7. Same as Figure 6, but for magnetic-to-fluid pressure ratio β^{-1}.

radial fluid motion, which is orthogonal to the magnetic field lines in this region as a result of the dipole geometry. The resulting "trapped zone" extends to $r \approx 50$ km.

To understand the wind dynamics better, Figure 11 shows the cumulative change of various energies interior to a given radius above the PNS surface, over the ≈55 ms duration of the simulation, again broken down separately into polar (left panel) and equatorial angular sectors (right panel). In both latitude ranges, the increase in the magnetic energy (black lines) exceeds the increases in the wind's thermal (green lines) or kinetic (blue lines) energies. This illustrates that most of the energy deposited by neutrino heating (red lines) is used to open magnetic field lines, rather than powering the wind. The energy being expended to open field lines is not available to unbind matter from the gravitational potential well of the PNS and hence contributes to the initial suppression of the wind mass-loss rate and kinetic power shown in Figure 5. Indeed, the magnetic energy rises with a greater delay in the equatorial belt relative to the polar regions, because it takes longer to open the closed magnetic field lines at lower latitudes (which are initially oriented perpendicular to the fluid flow) through neutrino heating. This is counterbalanced by a greater fraction of the neutrino-heating rate being deposited into thermal energy in the equatorial region (the ratio of the black to red lines in Figure 5) compared to the polar region, because of the longer residence time of the matter trapped in the closed portion of the magnetosphere compared to the expansion time of a continuous

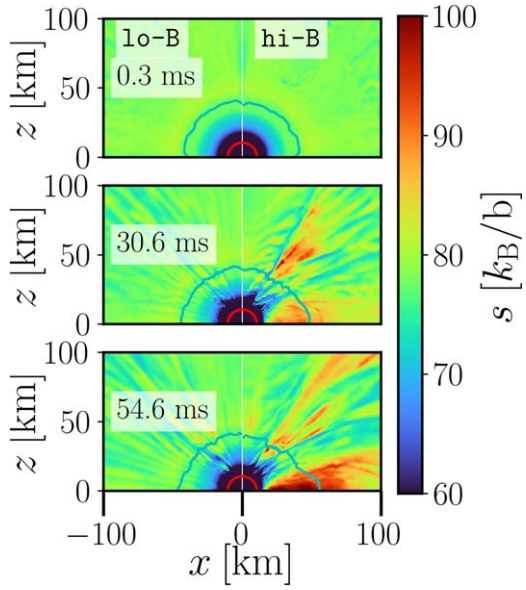

Figure 8. Same as Figure 7, but for specific entropy s. The effect of the enhanced heating of matter in the equatorial closed zone is apparent.

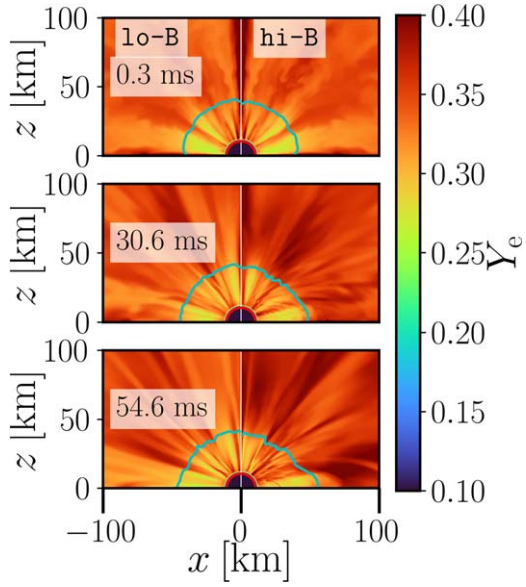

Figure 9. Same as Figure 7, but for Y_e.

outflow. Moreover, the "equatorial" region corresponding to Figure 5 is defined as the broad angular sector with polar angle $\theta = 45°$–$90°$; polar outflowing material is diverted by field lines to the equatorial angular sector, which contributes to the steady rise in equatorial $\dot{M}_{\rm iso}$.

The trapped zone is further illustrated by Figure 12, which shows the total specific energy of the fluid

$$E_{\rm tot} = -h' u_t - 1, \tag{6}$$

where we have now modified the specific enthalpy h to include the effects of magnetic tension according to

$$h' = 1 + \epsilon + \frac{P_f - P_{B,\rm T}}{\rho}. \tag{7}$$

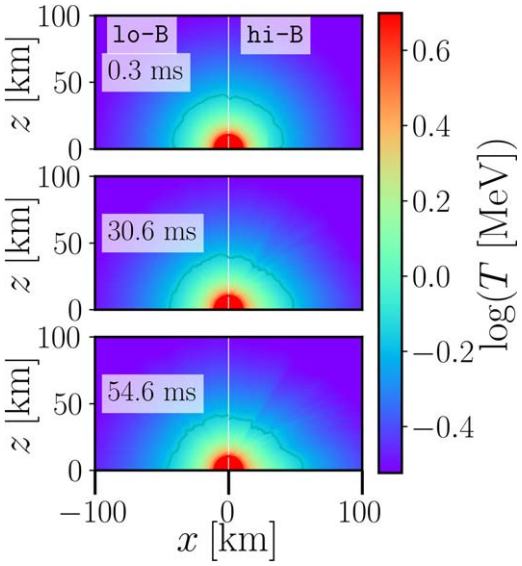

Figure 10. Same as Figure 7, but for temperature T.

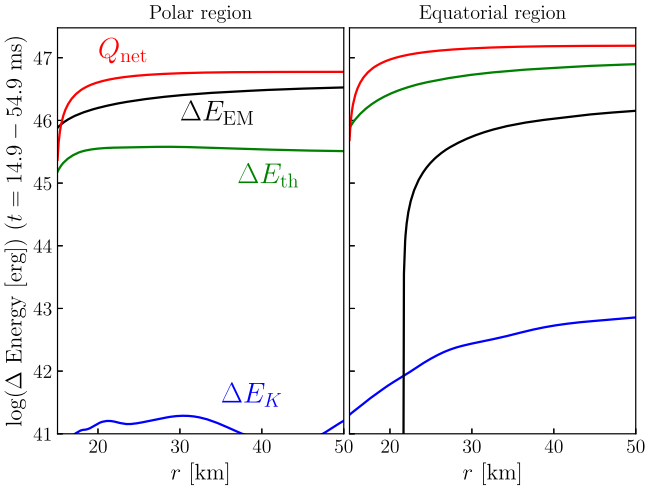

Figure 11. Change in the energy contained within the volume extending from $r = 15$ km to an outer radius r between $t \approx 15$ ms and $t \approx 55$ ms following the initialization of the magnetic field for model `hi-B`. Left: polar component, averaged azimuthally and over polar angles $\theta = 0°$–$45°$ and $135°$–$180°$. Right: equatorial component, averaged azimuthally and over polar angles $\theta = 45°$–$135°$. The energies are defined as follows: kinetic energy $E_K = \int (W-1)\rho W\sqrt{\gamma}\, d^3x$ (blue); thermal energy $E_{\rm th} = \int \epsilon\rho W\sqrt{\gamma}\, d^3x$ (green); electromagnetic energy $E_{\rm EM} = \int n_\mu n_\nu T^{\mu\nu}_{\rm EM}\sqrt{\gamma}\, d^3x$ (black); and net integrated neutrino heating $Q_{\rm net} = \int\int \dot{q}_{\rm net}\rho W\sqrt{\gamma}\, d^3x\, dt$ (red). Here, $T^{\mu\nu}_{\rm EM}$ is the electromagnetic stress–energy tensor, n^μ is the four-velocity of the Eulerian observer, W is the Lorentz factor associated with the total four-velocity, and γ is the determinant of the three-metric. The specific net neutrino-heating rate $\dot{q}_{\rm net}$ is integrated over the time interval; all other quantities are evaluated at the final and initial times, with their difference plotted.

Here, u_t is the 0-component of the four-velocity, ϵ is the specific internal energy, and

$$P_{B,\rm T} \equiv \sin\alpha \frac{B^2}{4\pi}\left(\frac{R_\nu}{R_c(r,\theta)}\right), \tag{8}$$

is the effective confining pressure of magnetic tension, where α is the local angle between the radial direction and the magnetic field line direction and R_c is the radius of curvature. The bound region $E_{\rm tot} < 0$ under this definition extends to 50 km in equatorial regions for model `hi-B`, consistent with the

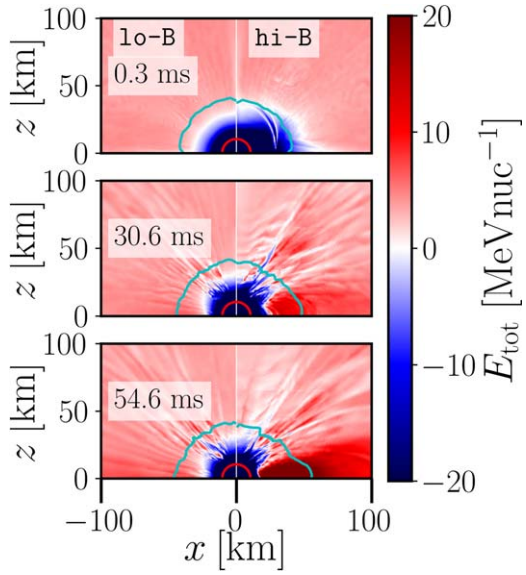

Figure 12. Same as Figure 7, but for the total specific energy $E_{\rm tot}$, including the effects of magnetic tension (Equation (6)). The energy grows in the equatorial belt due to neutrino heating of matter trapped in the closed zone, becoming positive by the final snapshots across a greater region extending to smaller radii approaching the PNS surface. As this high-entropy matter expands through the seed formation region (outside the cyan contour) it can potentially generate the conditions necessary for second- or third-peak *r*-process nucleosynthesis.

geometry of a trapped zone evident in the velocity field as discussed above (Figure 6).

Since the neutrino properties are not significantly altered by the strong magnetic field, the gain region remains almost identical to that in models `no-B` and `lo-B`, starting at the PNS surface and extending out to ≈50 km. As a result, the trapped zone experiences additional neutrino heating, increasing the ratio of fluid pressure to magnetic tension pressure (Figure 7). Unlike for the quasi-steady-wind solutions achieved in models `no-B` and `lo-B`, the specific entropy in the trapped magnetosphere, $\Delta s = \int \dot{q}_{\rm net}/Tdt$, thus rises monotonically with time (Figure 8).

Eventually, once the trapped zone is heated sufficiently for the fluid pressure to exceed the magnetic pressure, the field lines should open and the high-entropy matter will be ejected. The timescale over which this occurs, $t_{\rm ej}$, can be estimated by (e.g., Thompson 2003; Thompson & ud-Doula 2018)

$$t_{\rm ej} = \frac{P_{B,\rm T} - P_f}{\dot{q}_{\rm net}\rho}. \quad (9)$$

The top panel of Figure 13 shows the ejection time $t_{\rm ej}$ (Equation (9)) computed for model `hi-B` at two times: just after the magnetic field is initialized (left panel) and at a snapshot taken ≈31 ms later (right panel). Initially, $t_{\rm ej}$ peaks in the equatorial belt above the PNS surface at a value $\simeq$ 50 ms. By ≈31 ms the trapped region has shrunk in size, and the maximum ejection time has dropped to $t_{\rm ej} \simeq 20$ ms, roughly as expected given the amount of time elapsed. The entropy of the trapped-zone material at the time of ejection $t = t_{\rm ej}$ can be estimated as (e.g., Thompson 2003)

$$s_{\rm proj} \approx s + t_{\rm ej}\dot{q}_{\rm net}/T, \quad (10)$$

where $t_{\rm ej}\dot{q}_{\rm net}/T$ is the projected entropy gain at the approximate time of ejection (Equation (9)). The bottom panel of Figure 13 compares this future-projected final entropy $s_{\rm proj}$ at the time of

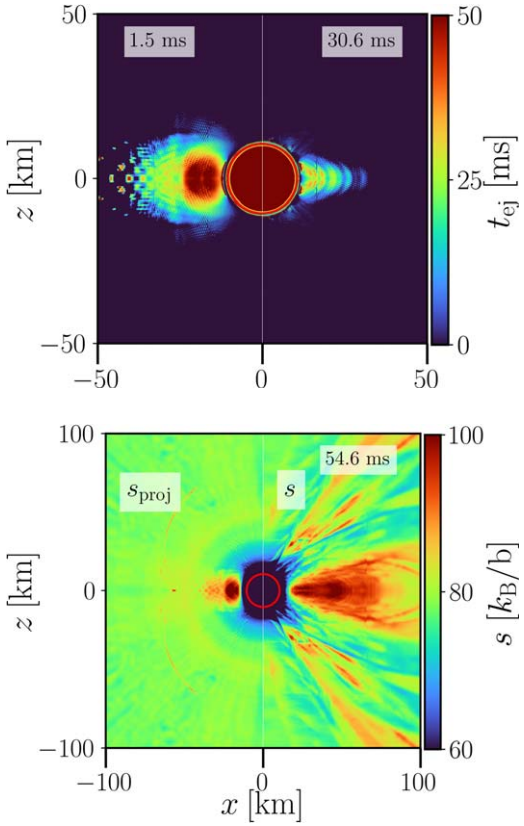

Figure 13. Top: closed-zone ejection timescale $t_{\rm ej}$ (Equation (9)) computed just after magnetic field initialization (left) and 30 ms later (right) for model `hi-B` in a slice through the $y = 0$ plane. Bottom: snapshots from model `hi-B` showing (left) the final entropy $s_{\rm proj}$ of the closed-zone material achieved after a time $t_{\rm ej}$ (Equation (9) from Thompson 2003 applied to the initial snapshot) in comparison to (right) the actual entropy s from the simulation at $t \approx 55$ ms after magnetic field initialization. The red contour represents the neutrinosphere surface ($\tau_{\bar{\nu}_e} = 1$). The analytic estimate is roughly consistent with the actual entropy achieved in the trapped zone of the wind.

magnetic field initialization (left panel) to the actual entropy achieved $t_{\rm ej} \approx 55$ ms later (right panel), around when trapped-zone material is expected to be ejected. The fact that the maximum value of the entropy achieved in the equatorial region roughly agrees with the projected entropy $s_{\rm proj}$ in this region, suggests that complete ejection of the closed zone is imminent by the end of our simulation.

Unlike the equatorial region, the polar region is not trapped by the magnetic field; thus the material there does not experience additional heating and the entropy of the outflowing material is similar to that obtained in the weakly magnetized models `lo-B` and `no-B` (Figure 8). The bottom panel of Figure 5 shows for model `hi-B` how the entropy in the equatorial region at radius ≈60 km grows in time (solid red line, bottom panel) in comparison to the roughly constant entropy of `lo-B` and `no-B` (blue and black lines, respectively) and for polar outflows in model `hi-B`. Given the neutrino luminosities/energies and the strength of the magnetic field of our simulations, the entropy gain we find agrees with that found by Thompson & ud-Doula (2018; see their Figure 5).

Figure 8 shows that the α-particle formation surface (cyan contour) passes through the equatorial trapped-zone region. Thompson & ud-Doula (2018) found that the neutrino heating of material in the trapped zone increases the ratio of gas-to-magnetic pressure until a minimum β^{-1} is reached, after which

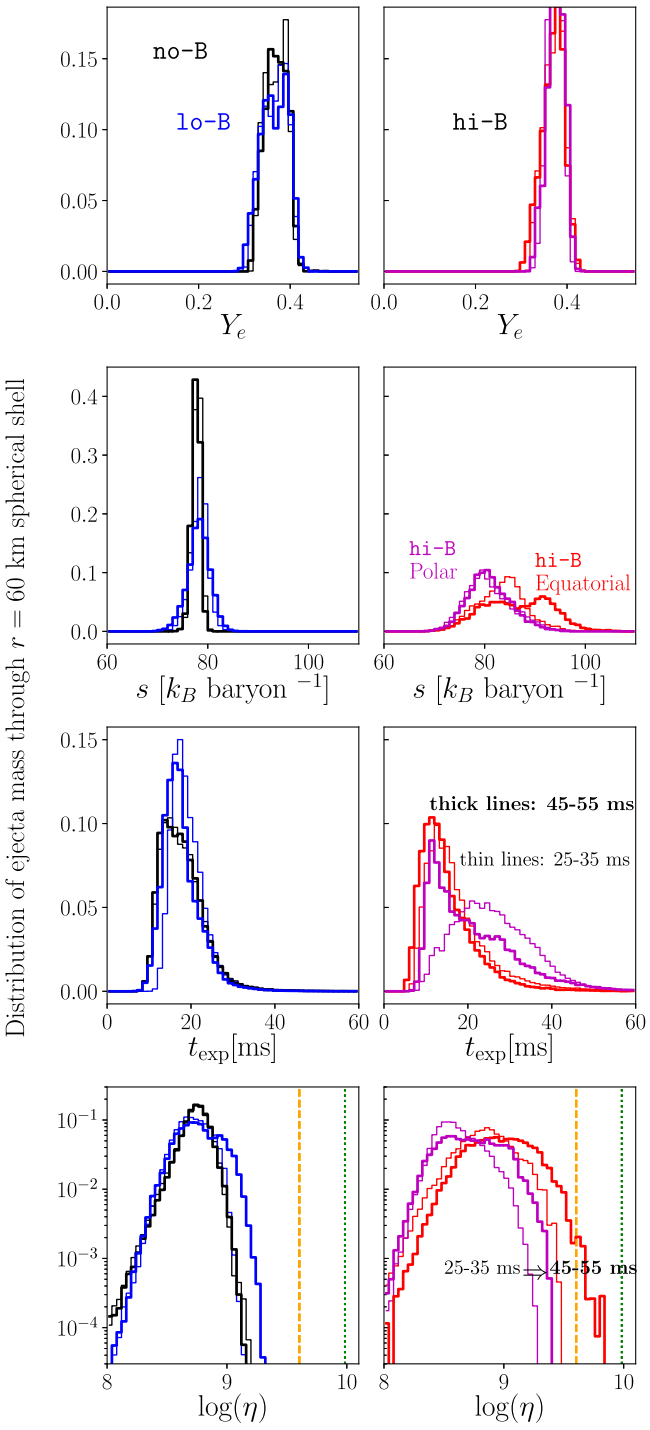

Figure 14. Histograms of various quantities relevant to *r*-process nucleosynthesis as measured through a 60 km spherical shell. The left panel shows the unmagnetized (`no-B`, black) and weakly magnetized (`lo-B`, blue) models, while the strongly magnetized model (`hi-B`) is shown on the right, broken down separately into the polar (purple) and equatorial (red) outflows, respectively (defined over the same angular domains as in Figure 5). For the unmagnetized models we show the results over the full time interval 25–55 ms, because the outflow is approximately time stationary, while for the magnetized models we separately bin results for 25–35 ms (thin lines) and 45–55 ms (thick lines). At a given time, the quantities are weighted pointwise on the spherical grid by the local mass outflow, where they are binned and normalized by the total mass outflow through the entire surface over the time interval. We approximate the outflow expansion time (Equation (4)) as $t_{\rm exp} = R/v(R)$, where $v(R)$ is the total wind speed measured at the shell. Threshold values for η (Equation (5)) required for neutron captures to reach the second (yellow dashed vertical line) and third (green dotted vertical line) *r*-process peaks (Hoffman et al. 1997) are indicated for comparison.

the closed zone is ejected as a single coherent structure. In our `hi-B` model we find that material from the trapped zone already has begun to leak out by $t \gtrsim 35$ ms. We speculate that the energy released by α-particle recombination, neglected by Thompson & ud-Doula (2018), contributes to unbinding matter from the edge of the closed zone in our simulation, in addition to neutrino heating.

3.3. Implications for r-process Nucleosynthesis

Figure 14 shows angle- and time-sampled histograms of the outflow properties relevant to *r*-process nucleosynthesis as measured through a spherical surface of radius ≈60 km for models `no-B` and `lo-B` (left column). We also show the results for model `hi-B` (right column), in this case broken down separately into polar and equatorial outflows and (since the highly magnetized case has not reached a steady state) shown in separate time intervals 25–35 ms and 45–55 ms after activation of the magnetic field, respectively. Some of these time-averaged wind properties are also summarized in Table 2.

The Y_e distributions for all models are isotropic and nearly identical to one another (see also Figure 9); this is as expected because the outflow speeds are sufficiently low that neutrino absorptions have time to bring Y_e into equilibrium, and as already mentioned, the properties of the neutrino radiation are similar between the magnetized and unmagnetized models (Table 1). The entropy distributions for the weakly magnetized models `lo-B` and `no-B` are nearly identical to each other, centered around $s \approx 78$ with a relatively narrow spread of $\Delta s \approx \pm 1$ (Table 2). This is also as expected given the previously noted similarities between the unmagnetized and weakly magnetized models, for both of which the outflow reaches an approximate steady state (Section 3.1).

In the strongly magnetized model `hi-B`, the entropy distribution of the polar outflows overlaps that of the weakly magnetized case, though with a significantly larger spread $\Delta s \approx \pm 3.6$. By contrast, the mean entropy of the equatorial `hi-B` outflows is shifted to a higher value $s \gtrsim 80$, with an even greater spread $\Delta s \approx \pm 6$ in the distribution. Furthermore, the mean entropy rises significantly in time (compare the 25–35 ms versus 45–55 ms samples in Figure 14), such that by the end of the simulation values as high as $s \gtrsim 100$ are achieved (see also Figure 8).

The expansion timescale distribution for models `lo-B` and `no-B` are again nearly identical, centered around ∼20 ms. For both the polar and equatorial ejecta in model `hi-B` the distribution extends to larger expansion times than the weakly magnetized cases, due to the significant trapping effect of the magnetic field. The nearly indistinguishable $\{Y_e, s, t_{\rm exp}\}$ distributions between models `lo-B` and `no-B` imply that the distributions of η (Equation (5)) should also agree; this is seen in the bottom panel of Figure 14. As already noted (Section 3.1), both models remain well below the required threshold η for second-peak *r*-process production.

By contrast, for the strongly magnetized model `hi-B`, the η distribution of the equatorial outflows extend to higher values due to the higher entropy ($\eta \propto s^3$). Over the course of the simulation, η increases from a mean value of $\approx 4 \times 10^8$ to $\approx 1 \times 10^9$, with the high-η tail (about 0.4% of the equatorial material) achieving values $\gtrsim 4 \times 10^9$ necessary for second-peak *r*-process production ≈45–55 ms after the magnetic field is initialized. We conclude that—all else being equal (e.g., in terms of their neutrino emission properties)—strongly

magnetized PNSs are more promising *r*-process sources than weakly magnetized PNS.

The outflow entropies for our model `hi-B` are broadly consistent with those found by Thompson & ud-Doula (2018) using 2D axisymmetric MHD simulations, for roughly the same surface magnetic field strength. These authors also found that a small fraction of the ejecta reaches large values of $\eta \gtrsim 10^{10}$, sufficient for a second- or even third-peak *r*-process, due to the transient ejection of high-entropy matter from the closed zone. Although the evolution of our `hi-B` model indeed resembles a single episode of closed-zone inflation and eruption, our simulations unfortunately cannot be run as long as those by Thompson & ud-Doula (2018) and Prasanna et al. (2022) due to the higher computational cost of our 3D GRMHD simulations that aim to resolve the neutrinosphere marginally, versus axisymmetric 2D simulations.

Beyond their computational cost, the duration of our simulations are also limited by numerical issues: at late times $t \gtrsim 60$ ms, spurious violations of $\nabla \cdot \boldsymbol{B} = 0$ at the refinement level boundaries of our fixed Cartesian grid hierarchy of concentric boxes at a level of $\sim$1% have accumulated due to interpolation operations over a total of $\gtrsim$210 ms of evolution and residual violations introduced by initializing the large-scale dipole magnetic field. At this level, we do not entirely trust the subsequent results and choose not to consider those data in our analyses, even though the conditions for heavy *r*-process nucleosynthesis are seen to be improving with time as higher-entropy material expands through the seed formation region. We refer to Appendix A.5 for a more detailed discussion of the issue of $\nabla \cdot \boldsymbol{B} = 0$ violation.

4. Summary and Conclusions

We have performed 3D GRMHD simulations including M0 neutrino transport of magnetized PNS winds to explore the impact that magnetar-strength dipole surface magnetic fields have on the outflow properties, with a particular focus on the conditions necessary for a successful *r*-process via the α-rich freeze-out mechanism in mildly neutron-rich winds. Our results can be summarized as follows.

1. For even the strongest magnetic fields that we consider ($B_S = 2.5 \times 10^{15}$ G; model `hi-B`), magnetic forces do not appreciably impact the hydrostatic structure of the wind near the neutrinosphere radii. As a result, the properties of the neutrino radiation (L_ν, E_ν, R_ν) which dictate the equilibrium electron fraction and specific heating rate in the gain region, are similar between the magnetized and unmagnetized models.
2. In the case of a relatively weak magnetic field ($B_S \simeq 6.1 \times 10^{14}$ G; $B_S < B_{crit}$; model `lo-B`) for which $\beta^{-1} = P_B/P_f \lesssim 1$, the dipole field structure is torn open by neutrino-driven outflows within $\sim$10 ms, and the magnetic field takes on a split-monopole configuration by $\approx$40 ms (Figures 3 and 4). Outflow properties such as the mass-loss rate and entropy are approximately spherical and quantitatively similar to those from the otherwise similar unmagnetized PNS model `no-B` (e.g., Figures 2 and 14).
3. In stark contrast, the wind structure of the highly magnetized model ($B_S \simeq 2.5 \times 10^{15}$ G; $B_S > B_{crit}$; model `hi-B`) differs qualitatively from the weakly magnetized cases. The outflows that emerge along the polar axis of the dipole follow open magnetic field lines and are broadly similar in their isotropic-equivalent properties to the spherical unmagnetized and weakly magnetized winds. One exception is the isotropic mass-loss rate, which is initially suppressed compared to a weakly magnetized wind, because a significant portion of the energy deposition from neutrino heating goes into opening polar magnetic field lines rather than lifting matter out of the gravitational potential of the star (Figure 11). Furthermore, as a result of opening up field lines, a fraction of the polar outflows are diverted toward intermediate latitudes in the equatorial region, which enhances the equatorial isotropic-equivalent mass flux.

   By contrast, outflowing material in the equatorial regions of the wind are initially trapped by the nonradial magnetic field at lower latitudes (Figures 5, 6, and 13), with the magnetosphere in this region maintaining a dipole field structure well above the PNS surface (Figure 3). Neutrino heating raises the thermal pressure of the trapped fluid in the equatorial region until it obeys $P_f > P_B$ (Thompson 2003; Prasanna et al. 2022), at which point fluid begins to escape and the closed zone begins to shrink from the outside inwards. Energy input from α-particle formation appears to aid the ejection of matter from the equatorial regions, and by the end of the simulation the isotropic-equivalent mass-loss rate even slightly overshoots that of the otherwise equivalent unmagnetized wind (Figure 5).
4. The weakly magnetized wind model achieves a rough steady state and does not show significant entropy growth relative to the unmagnetized model, because matter is not trapped by the magnetic field (Figure 2, top panel; Figure 5, bottom panel). By contrast, plasma trapped in the strongly magnetized model causes the mean entropy of the trapped and eventually outflowing material from the equatorial region to rise, with its standard deviation grows concurrently (Figure 14, second row, right panel), over the course of $\sim$50–60 ms. The mean expansion time of the equatorial outflows through the seed formation region is also moderately larger compared to the weakly magnetized cases because of the suppressed outflow speed.
5. For the strongly magnetized model, the heating profile and magnetic field strength in the trapped equatorial belt imply an ejection timescale of the trapped plasma of $\sim$50 ms, following the analytic estimates of Thompson & ud-Doula (2018; Figure 13); although we do not see a discrete ejection event, a continuous slow but accelerating "peeling" of the trapped zone is observed to occur on this timescale. The projected entropy gain (Thompson 2003) broadly agrees with the rise in entropy we observe in the simulation.
6. The *r*-process figure-of-merit parameter η for unmagnetized and weakly magnetized models are similar ($\lesssim 10^9$), remaining well below the required threshold ($\approx 4 \times 10^9$) to produce second-peak *r*-process elements (Figure 14). By contrast in the strongly magnetized model, due to the monotonic rise in the mean entropy of the equatorial outflows (particularly a "tail" of matter extending to high entropy $s \gtrsim 100$), sufficiently high η may be achieved for a small subset ($\approx$0.4%) of equatorial material, within $\sim$50 ms of magnetic field initialization. Following this

trend to later times than the duration of our simulation, we conclude that a moderate fraction of the time-averaged wind material could well attain values of η that surpass the second and potentially also third r-process peaks. Though due to numerical limitations we cannot follow the multiple cycles of trapped-zone inflation and mass ejection seen by Thompson & ud-Doula (2018) and Prasanna et al. (2022), our results are in broad agreement with the findings of these authors.

Paper I demonstrated that rapid rotation in unmagnetized PNS winds tends to reduce the entropy of neutrino-driven outflows, while in the present paper we have shown that a strong magnetic field tends to increase the wind entropy. Although some aspects of the phenomena we have studied will be "additive" (i.e., neutrino-heating-driven ejections from a rotating magnetosphere), qualitatively new features of the wind properties, such as magneto-centrifugal acceleration, are expected to emerge through the combined impact of rapid rotation and strong magnetic fields (e.g., Thompson et al. 2004; Metzger et al. 2007; Vlasov et al. 2017; Prasanna et al. 2022; Combi & Siegel 2023b; Prasanna et al. 2023; Raives et al. 2023). Rotating protomagnetar winds will be the focus of future work.

Acknowledgments

We thank Erik Schnetter, Roland Haas, and Luciano Combi for discussions and support. This research was enabled in part by support provided by SciNet (www.scinethpc.ca) and Compute Canada (www.computecanada.ca). The authors gratefully acknowledge the computing time granted by the Resource Allocation Board and provided on the supercomputer Lise and Emmy at NHR@ZIB and NHR@Göttingen as part of the NHR infrastructure. The calculations for this research were conducted with computing resources under the project mvp-00022. D.K.D. and B.D.M. acknowledge support from the National Science Foundation (grant #AST-2002577). D.M.S. acknowledges the support of the Natural Sciences and Engineering Research Council of Canada (NSERC), funding reference number RGPIN-2019-04684. Research at Perimeter Institute is supported in part by the Government of Canada through the Department of Innovation, Science and Economic Development Canada and by the Province of Ontario through the Ministry of Colleges and Universities.

Software: The Einstein Toolkit (Löffler et al. 2012; http://einsteintoolkit.org), GRMHD_con2prim (Siegel & Mösta 2018), PyCactus (Kastaun 2021), Matplotlib (Hunter 2007), NumPy (Harris et al. 2020), SciPy (Virtanen et al. 2020), and hdf5 (The HDF Group 1997–2022).

Appendix
Numerical Tests

This appendix presents a number of tests we have performed on the simulation results, which justify simplifications made in the grid setup and assumptions regarding the microphysics we have included.

A.1. Spatial Resolution

Figure 15 shows the vertical scale height of the magnetic field strength B and neutrino optical depth $\tau_{\bar{\nu}_e}$ as a function of radius for the strongly magnetized model `hi-B`. We resolve the magnetic field by at least 10 grid points throughout the entire simulation domain. The same conclusion holds for model `lo-B`.

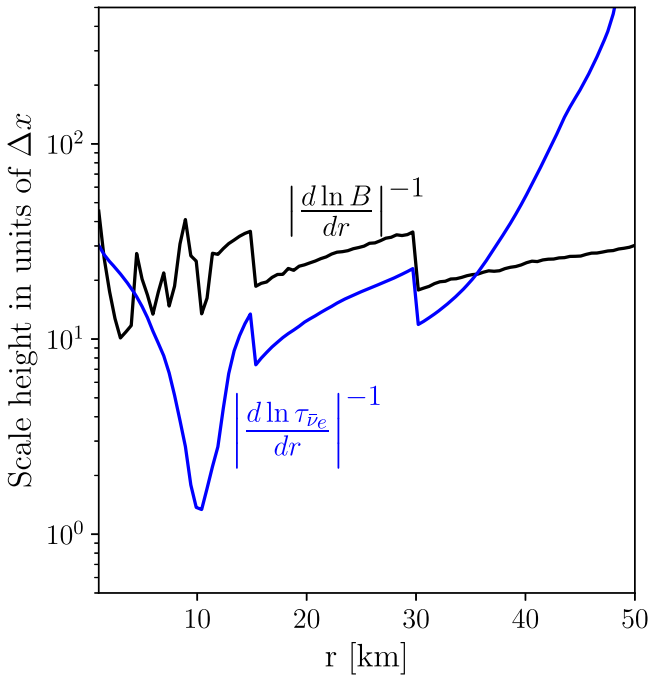

Figure 15. Vertical scale height as a function of radius of the magnetic field B (black) and neutrino optical depth $\tau_{\bar{\nu}_e}$ (blue) for model `hi-B`, normalized by the grid step size Δx. The radial profiles correspond to a slice through the magnetic dipole axis ($y = 0$ plane), averaged over the polar angle between $\theta = 0°$ and $\theta = 45°$, and time averaged over the first 4 ms after the magnetic field is initialized. The discontinuities at 15 km and 30 km reflect refinement level boundaries.

Although we only marginally resolve the neutrinosphere with $\approx$1 grid point per scale height at radii where $\tau_{\bar{\nu}_e} \sim 1$, the main effect of this deficiency is on the properties (luminosity and mean energy) of the escaping neutrino flux (Paper I). Although the asymptotic electron fraction of the wind is very sensitive to these properties, the main focus of this study is on the effects of a strong magnetic field for an otherwise fixed neutrino radiation field (and the neutrino properties do not depend strongly on the magnetic field; see Table 1). Furthermore, at larger radii, specifically in the gain region where the net neutrino heating launches the wind, we do sufficiently resolve the optical depth scale height. For the purposes of this study, the resolution of our simulations is therefore sufficient to capture magnetic field effects and bulk wind dynamics.

A.2. Hemisphere Symmetry Assumption

We perform two otherwise identical simulations, with and without imposing reflection symmetry across the equatorial ($z = 0$) plane, to check that the results of the half-hemisphere simulations presented in this paper are independent of the use of this assumption (`no-sym-B` and `sym-B`, Table 1). The two simulations use the same refinement level box sizes as those of our fiducial models, but with the resolution of the smallest refinement level being 450 m rather than 150 m, for reasons of computational expense associated with the full-domain simulations. The setup of the two models is similar to the fiducial magnetized models: after reaching roughly steady-state wind properties with zero magnetic field, we initialize a dipole

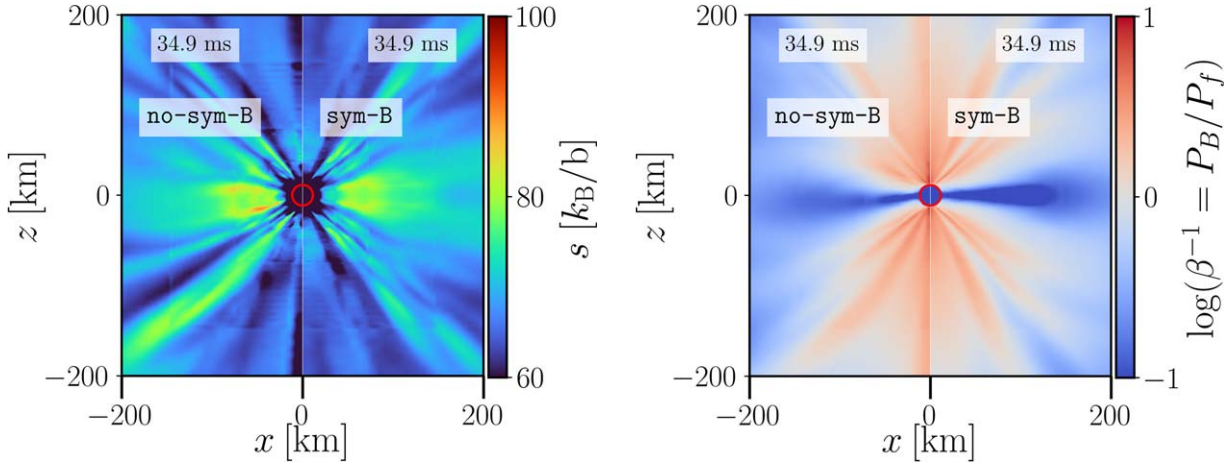

Figure 16. Comparison of wind properties with and without imposing reflection symmetry across the equatorial plane. Shown are wind cross sections in the plane of the magnetic dipole axis for specific entropies (left panel) and magnetic-to-fluid pressure ratios (right panel) time averaged over the interval $t \simeq 30$–35 ms after the B-field is initialized. For each panel the simulation is run across the full $\theta \in [0, \pi]$ domain (left; model `no-sym-B`) and reflection symmetry across the $z = 0$ plane is employed (right; model `sym-B`).

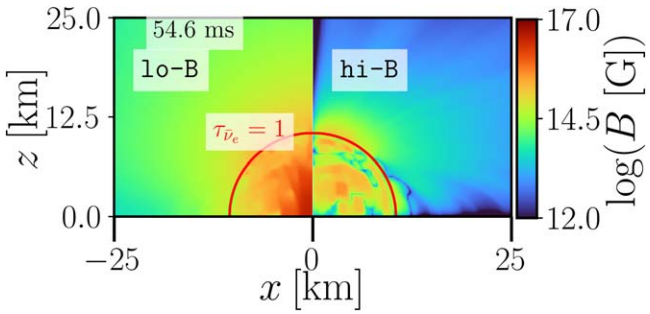

Figure 17. Strength of the poloidal (left) and toroidal (right) magnetic field components for model `hi-B` approximately 55 ms after initialization of the magnetic field. The red contour indicates the location of the neutrinosphere.

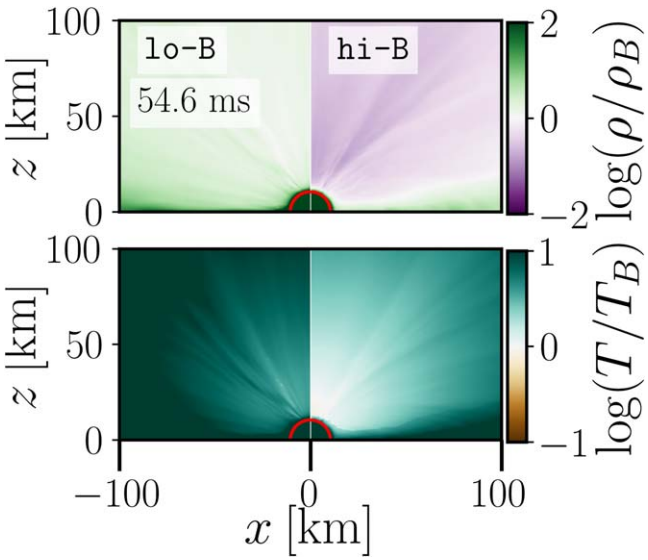

Figure 18. Cross section of the $y = 0$ magnetic dipole axis plane for the `lo-B` (left) and `hi-B` runs (right) ≈55 ms after the magnetic field is initialized, showing the ratios of the temperature T (top) and density ρ (bottom) to their respective critical values T_B and ρ_B below which quantizing effects of the magnetic field on the equation of state and weak interactions are expected (Equations (11) and (12)). Since $T/T_B > 1$ everywhere, electrons and positrons populate many Landau levels, even in the regime where $\rho < \rho_B$. The magnetic winds are thus in the nonquantizing regime, justifying our negligence of magnetic field effects on the equation of state and weak interactions. The red contour indicates the $\tau_{\bar{\nu}_e} = 1$ neutrinosphere surface.

magnetic field of strength $B_S \approx 2.2 \times 10^{15}$ G and further evolve the models for ≃40 ms.

Broadly, the temporal evolutions of the two simulations are qualitatively similar to those of the `hi-B` model ($B_S = 2.5 \times 10^{15}$ G): a thin reconnection layer with a low magnetic-to-fluid pressure ratio β^{-1} forms in the equatorial plane, and high β^{-1} in the polar region due to magnetic field lines being torn open and approaching a split-monopole-like solution in that region. The half- and full-domain simulations are even more similar to each other. Figure 16 shows a snapshot comparing the magnetic-to-fluid pressure ratio roughly 35 ms after the magnetic field has been initialized. Although the low β^{-1} equatorial current sheet/reconnection layer becomes slightly warped in the full-domain simulation (perhaps due to reconnection-related instabilities), the reconnection layer appears nearly symmetric and similar to the half-domain simulation when time averaged over a 20 ms interval. We conclude that while our half-domain simulation may miss some features of the dynamics near the equatorial plane, the time-averaged wind properties will not be greatly effected by this simplification.

A.3. Toroidal Field

Absent any large-scale nonradial motions (due, e.g., to rotation), or the presence of other nonaxisymmetric instabilities such as convection, we should expect the strength of the toroidal component of the magnetic field, B_T, to remain highly subdominant compared to the poloidal field, B_P. We check this expectation in Figure 17 by showing B_T and B_P from a snapshot of our `hi-B` model at 60 ms. The ratio B_T/B_P achieves a maximum value 10^{-1} inside the PNS, but has typical values $\lesssim 10^{-2}$ outside the neutrinosphere everywhere else on the grid. As expected, the toroidal field should thus have no appreciable impact on the wind dynamics in the case of a nonrotating PNS.

A.4. Landau Level Effects

Strong magnetic fields modify neutrino absorption and emission rates as well as the equation of state via quantization

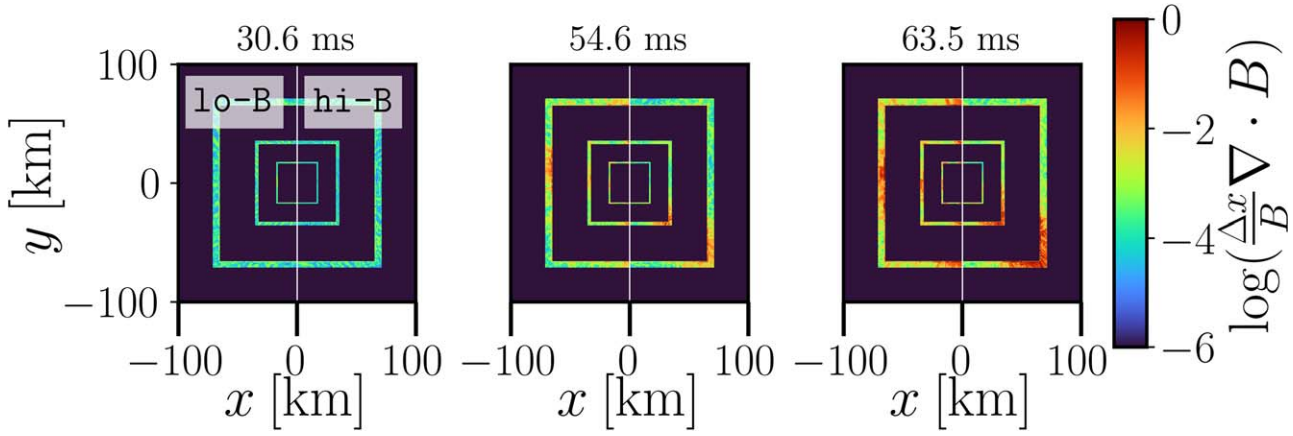

Figure 19. Equatorial plane ($z = 0$) cross section at three snapshots in time (≈31 ms, 55 ms, 64 ms after dipole magnetic field initialization) for models `lo-B` (shown in the $x < 0$ domain) and `hi-B` (shown in the $x > 0$ domain). The color represents the relative level of $\nabla \cdot \boldsymbol{B}$ violations, where Δx is the grid spacing, and B is the overall strength of the magnetic field. While the constraint transport scheme maintains $\nabla \cdot \boldsymbol{B}$ to machine precision interior to the refinement level boundaries, spurious violations are introduced at the refinement boundaries due to interpolation operations.

of the electron and positron energy levels resulting from the quantization into Landau levels of $e^{\pm}$ motion transverse to the magnetic field (Lai & Qian 1998; Duan & Qian 2004, 2005). Such modifications become irrelevant for temperatures $T \gtrsim T_B$ or $\rho \gg \rho_B$, where T_B is the critical temperature

$$T_B = \begin{cases} \dfrac{m_e c^2}{k_B}\left(\sqrt{\dfrac{2B}{B_{\rm Q}} + 1} - 1\right) & \text{for } \rho \leqslant \rho_B, \\ \dfrac{\hbar \omega_c}{k_B}(1 + x_F^2)^{-1/2} & \text{for } \rho \gg \rho_B, \end{cases} \tag{11}$$

and ρ_B is the critical density

$$\rho_B = 2.23 \times 10^9 \left(\frac{Y_e}{0.1}\right)^{-1} \left(\frac{B}{10^{15}\ \mathrm{G}}\right)^{3/2} \mathrm{g\ cm^{-3}}, \tag{12}$$

defined as the density below which only the ground Landau level is populated by electrons (Harding & Lai 2006; Haensel et al. 2007). Here, m_e is the electron mass, c is the speed of light, $\omega_c = eB/(m_e c)$ is the cyclotron frequency, $x_F = (\hbar/m_e c)(3\pi^2 Y_e \rho/m_{\rm u})^{1/3}$ is the normalized relativistic Fermi momentum, $m_{\rm u}$ is the atomic mass unit, and $B_{\rm Q} = 4.414 \times 10^{13}$ G is the critical QED magnetic field strength (obtained by equating the cyclotron energy of an electron to $m_{\rm ec}^2$). If either the density or temperature is larger than their respective critical values, the $e^{\pm}$ distributions extend over many Landau levels and the magnetic field does not have a quantizing effect. Figure 18 shows the ratios T/T_B and ρ/ρ_B of our magnetized runs once a stationary PNS wind has emerged. Since $T > T_B$ everywhere, the magnetic field is nonquantizing, even in the polar regions where $\rho < \rho_B$, justifying our assumptions regarding the impact of magnetic fields on the equation of state and weak interactions.

A.5. Divergence-free Constraint Violations

The magnetic field in our simulations is evolved using the FluxCT method (Tóth 2000) to maintain the solenoidal constraint $\nabla \cdot \boldsymbol{B} = 0$ during evolution. While interior to the refinement level boundaries this constrained transport algorithm preserves $\nabla \cdot \boldsymbol{B}$ to machine precision, spurious violations are introduced over time at the refinement level boundaries due to interpolation during prolongation and restriction operations, which do not preserve $\nabla \cdot \boldsymbol{B}$ to machine precision. Although we use additional overlap zones at the refinement boundaries to minimize the impact of spurious violations on the evolution of the system, significant violations in ghost zones may impact the solution quantitatively beyond a certain timescale, which depends on the exact grid setup and the physical system. In the current case, spurious violations introduced during the first ∼150 ms of "preevolution" to establish a stationary, essentially unmagnetized wind (see Section 2), as well as violations introduced during magnetic field initialization and subsequent strongly magnetized evolution give rise to the spurious accumulation of errors at the refinement boundaries to the ∼1% level by ≳60 ms after the large-scale dipole magnetic field is initialized. Figure 19 illustrates the spurious growth of $\nabla \cdot \boldsymbol{B}$ at the refinement boundaries as a function of time after initialization of the dipole field. At ≈64 ms and onward, we consider the accumulated errors at the refinement level boundaries in the wind zone (∼60 km) prohibitive to trusting the results from subsequent evolution fully and thus choose not to include subsequent simulation data into our analyses. Preventing the effects of spurious $\nabla \cdot \boldsymbol{B}$ violations on the closed-zone material while maintaining the resolution requirements at the neutrinosphere (Appendix A.1) would require increasing the innermost box to ≈100 km. The associated increase in computational cost by a factor of $\sim(100/15)^3 \approx 300$ would render these simulations computationally infeasible.

ORCID iDs

Dhruv K. Desai https://orcid.org/0000-0002-8914-4259
Daniel M. Siegel https://orcid.org/0000-0001-6374-6465
Brian D. Metzger https://orcid.org/0000-0002-4670-7509

References

Arcones, A., Janka, H. T., & Scheck, L. 2007, A&A, 467, 1227
Arcones, A., & Montes, F. 2011, ApJ, 731, 5
Babiuc-Hamilton, M., Brandt, S. R., Diener, P., et al. 2019, The Einstein Toolkit (The "Mayer" release, ET_2019_10), Zenodo, doi:10.5281/zenodo.3522086
Barrère, P., Guilet, J., Reboul-Salze, A., Raynaud, R., & Janka, H. T. 2022, A&A, 668, A79
Beniamini, P., Hotokezaka, K., van der Horst, A., & Kouveliotou, C. 2019, MNRAS, 487, 1426

Bruenn, S. W. 1985, ApJS, 58, 771
Bucciantini, N., Quataert, E., Arons, J., Metzger, B. D., & Thompson, T. A. 2007, MNRAS, 380, 1541
Bucciantini, N., Quataert, E., Metzger, B. D., et al. 2009, MNRAS, 396, 2038
Bugli, M., Guilet, J., Foglizzo, T., & Obergaulinger, M. 2023, MNRAS, 520, 5622
Bugli, M., Guilet, J., & Obergaulinger, M. 2021, MNRAS, 507, 443
Burrows, A., Hayes, J., & Fryxell, B. A. 1995, ApJ, 450, 830
Burrows, A., & Lattimer, J. M. 1986, ApJ, 307, 178
Cantiello, M., Fuller, J., & Bildsten, L. 2016, ApJ, 824, 14
CHIME/FRB Collaboration, Andersen, B. C., Bandura, K. M., et al. 2020, Natur, 587, 54
Combi, L., & Siegel, D. M. 2023a, ApJ, 944, 28
Combi, L., & Siegel, D. M. 2023b, arXiv:2303.12284
Coti Zelati, F., Rea, N., Pons, J. A., Campana, S., & Esposito, P. 2018, MNRAS, 474, 961
Desai, D., Siegel, D. M., & Metzger, B. D. 2022, ApJ, 931, 104
Dessart, L., Burrows, A., Livne, E., & Ott, C. D. 2006, ApJ, 645, 534
Dessart, L., Ott, C. D., Burrows, A., Rosswog, S., & Livne, E. 2009, ApJ, 690, 1681
Duan, H., & Qian, Y.-Z. 2004, PhRvD, 69, 123004
Duan, H., & Qian, Y.-Z. 2005, PhRvD, 72, 023005
Duncan, R. C., Shapiro, S. L., & Wasserman, I. 1986, ApJ, 309, 141
Ferrario, L., & Wickramasinghe, D. 2006, MNRAS, 367, 1323
Fischer, T., Martínez-Pinedo, G., Hempel, M., & Liebendörfer, M. 2012, PhRvD, 85, 083003
Fischer, T., Whitehouse, S. C., Mezzacappa, A., Thielemann, F.-K., & Liebendörfer, M. 2010, A&A, 517, A80
Fuller, J., & Lu, W. 2022, MNRAS, 511, 3951
Fuller, J., Piro, A. L., & Jermyn, A. S. 2019, MNRAS, 485, 3661
Galeazzi, F., Kastaun, W., Rezzolla, L., & Font, J. A. 2013, PhRvD, 88, 064009
Giacomazzo, B., & Perna, R. 2013, ApJL, 771, L26
Goodale, T., Allen, G., Lanfermann, G., et al. 2003, in High Performance Computing for Computational Science — VECPAR 2002, 5th Int. Conf., ed. J. M. L. M. Palma et al. (Berlin: Springer), 197
Gossan, S. E., Fuller, J., & Roberts, L. F. 2020, MNRAS, 491, 5376
Haensel, P., Potekhin, A. Y., & Yakovlev, D. G. 2007, Neutron Stars 1 (1st ed.; New York: Springer)
Harding, A. K., & Lai, D. 2006, RPPh, 69, 2631
Harris, C. R., Millman, K. J., van der Walt, S. J., et al. 2020, Natur, 585, 357
Hoffman, R. D., Woosley, S. E., & Qian, Y.-Z. 1997, ApJ, 482, 951
Hunter, J. D. 2007, CSE, 9, 90
Janka, H.-T., Langanke, K., Marek, A., Martínez-Pinedo, G., & Müller, B. 2007, PhR, 442, 38
Kajino, T., Otsuki, K., Wanajo, S., Orito, M., & Mathews, G. J. 2000, in Few-Body Problems in Physics '99, ed. S. Oryu, S. Kamimura, & M. Ishikawa (Vienna: Springer), 80
Kaplan, J. D., Ott, C. D., O'Connor, E. P., et al. 2014, ApJ, 790, 19
Kaspi, V. M., & Beloborodov, A. M. 2017, ARA&A, 55, 261
Kastaun, W. 2021, PyCactus: Post-processing tools for Cactus computational toolkit simulation data, Astrophysics Source Code Library, ascl:2107.017
Kiuchi, K., Kyutoku, K., Sekiguchi, Y., & Shibata, M. 2018, PhRvD, 97, 124039
Kiuchi, K., Kyutoku, K., & Shibata, M. 2012, PhRvD, 86, 064008
Kouveliotou, C., Dieters, S., Strohmayer, T., et al. 1998, Natur, 393, 235
Kuroda, T., Arcones, A., Takiwaki, T., & Kotake, K. 2020, ApJ, 896, 102
Lai, D., & Qian, Y.-Z. 1998, ApJ, 505, 844
Löffler, F., Faber, J., Bentivegna, E., et al. 2012, CQGra, 29, 115001
Martínez-Pinedo, G., Fischer, T., Lohs, A., & Huther, L. 2012, PhRvL, 109, 251104
Metzger, B. D., Giannios, D., Thompson, T. A., Bucciantini, N., & Quataert, E. 2011, MNRAS, 413, 2031
Metzger, B. D., Thompson, T. A., & Quataert, E. 2007, ApJ, 659, 561
Metzger, B. D., Thompson, T. A., & Quataert, E. 2018, ApJ, 856, 101
Meyer, B. S., & Brown, J. S. 1997, ApJS, 112, 199
Meyer, B. S., Mathews, G. J., Howard, W. M., Woosley, S. E., & Hoffman, R. D. 1992, ApJ, 399, 656
Mösta, P., Mundim, B. C., Faber, J. A., et al. 2014, CQG, 31, 015005
Mösta, P., Ott, C. D., Radice, D., et al. 2015, Natur, 528, 376
Mösta, P., Radice, D., Haas, R., Schnetter, E., & Bernuzzi, S. 2020, ApJL, 901, L37
Nevins, B., & Roberts, L. F. 2023, MNRAS, 520, 3986
Obergaulinger, M., & Aloy, M. Á. 2021, MNRAS, 503, 4942
O'Connor, E., & Ott, C. D. 2010, CQG, 27, 114103
Otsuki, K., Tagoshi, H., Kajino, T., & Wanajo, S.-Y. 2000, ApJ, 533, 424
Perego, A., Rosswog, S., Cabezón, R. M., et al. 2014, MNRAS, 443, 3134
Pons, J. A., Reddy, S., Prakash, M., Lattimer, J. M., & Miralles, J. A. 1999, ApJ, 513, 780
Prasanna, T., Coleman, M. S. B., Raives, M. J., & Thompson, T. A. 2022, MNRAS, 517, 3008
Prasanna, T., Coleman, M. S. B., Raives, M. J., & Thompson, T. A. 2023, arXiv:2305.16412
Price, D. J., & Rosswog, S. 2006, Sci, 312, 719
Qian, Y., & Woosley, S. E. 1996, ApJ, 471, 331
Qian, Y.-Z., & Woosley, S. E. 1996, ApJ, 471, 331
Radice, D., Galeazzi, F., Lippuner, J., et al. 2016, MNRAS, 460, 3255
Raives, M. J., Coleman, M. S. B., & Thompson, T. A. 2023, arXiv:2302.05462
Raynaud, R., Guilet, J., Janka, H.-T., & Gastine, T. 2020, SciA, 6, eaay2732
Reboul-Salze, A., Guilet, J., Raynaud, R., & Bugli, M. 2022, A&A, 667, A94
Reichert, M., Obergaulinger, M., Aloy, M. Á., et al. 2023, MNRAS, 518, 1557
Roberts, L. F., & Reddy, S. 2017, in Handbook of Supernovae, ed. L. F. Roberts & S. Reddy (Cham: Springer), 1605
Roberts, L. F., Shen, G., Cirigliano, V., et al. 2012, PhRvL, 108, 061103
Roberts, L. F., Woosley, S. E., & Hoffman, R. D. 2010, ApJ, 722, 954
Ruderman, M. 1972, ARA&A, 10, 427
Ruffert, M., Janka, H.-T., & Schaefer, G. 1996, A&A, 311, 532
Schnetter, E., Hawley, S. H., & Hawke, I. 2004, CQG, 21, 1465
Shibata, M., Suwa, Y., Kiuchi, K., & Ioka, K. 2011, ApJL, 734, L36
Siegel, D. M., Ciolfi, R., Harte, A. I., & Rezzolla, L. 2013, PhRvD, 87, 121302
Siegel, D. M., Ciolfi, R., & Rezzolla, L. 2014, ApJL, 785, L6
Siegel, D. M., & Metzger, B. D. 2018, ApJ, 858, 52
Siegel, D. M., & Mösta, P. 2018, GRMHD_con2prim: a Framework for the Recovery of Primitive Variables in General-relativistic Magnetohydrodynamics, Zenodo, doi:10.5281/zenodo.1213306
Steiner, A. W., Hempel, M., & Fischer, T. 2013, ApJ, 774, 17
Sumiyoshi, K., Suzuki, H., Otsuki, K., Terasawa, M., & Yamada, S. 2000, PASJ, 52, 601
Suzuki, T. K., & Nagataki, S. 2005, ApJ, 628, 914
Takahashi, K., Witti, J., & Janka, H.-T. 1994, A&A, 286, 857
The HDF Group 1997-2022, Hierarchical Data Format, version 5
Thompson, C., & Duncan, R. C. 1993, ApJ, 408, 194
Thompson, T. A. 2003, ApJL, 585, L33
Thompson, T. A., Burrows, A., & Meyer, B. S. 2001, ApJ, 562, 887
Thompson, T. A., Chang, P., & Quataert, E. 2004, ApJ, 611, 380
Thompson, T. A., & ud Doula, A. 2018, MNRAS, 476, 5502
Thornburg, J. 2004, CQG, 21, 3665
Tóth, G. 2000, JCPH, 161, 605
Usov, V. V. 1992, Natur, 357, 472
Vink, J., & Kuiper, L. 2006, MNRAS, 370, L14
Virtanen, P., Gommers, R., Oliphant, T. E., et al. 2020, NatMe, 17, 261
Vlasov, A. D., Metzger, B. D., Lippuner, J., Roberts, L. F., & Thompson, T. A. 2017, MNRAS, 468, 1522
Wang, L., Howell, D. A., Höflich, P., & Wheeler, J. C. 2001, ApJ, 550, 1030
Weber, E. J., & Davis, L. J. 1967, ApJ, 148, 217
White, C. J., Burrows, A., Coleman, M. S. B., & Vartanyan, D. 2022, ApJ, 926, 111
Winteler, C., Käppeli, R., Perego, A., et al. 2012, ApJL, 750, L22
Woltjer, L. 1964, ApJ, 140, 1309
Woods, P. M., & Thompson, C. 2006, in Soft Gamma Repeaters and Anomalous X-ray Pulsars: Magnetar Candidates, ed. W. H. G. Lewin & M. van der Klis (Cambridge: Cambridge Univ. Press), 547
Woosley, S. E., Wilson, J. R., Mathews, G. J., Hoffman, R. D., & Meyer, B. S. 1994, ApJ, 433, 229